J. Fluid Mech. (2016), *vol.* 808, *pp.* 576–613.
doi:10.1017/jfm.2016.641

A numerical investigation of acceleration-skewed oscillatory flows

Pietro Scandura[1],†, **Carla Faraci**[2] **and Enrico Foti**[1]

[1]Department of Civil Engineering and Architecture, University of Catania, Via Santa Sofia 64, 95123 Catania, Italy

[2]Department of Engineering, University of Messina, Contrada Di Dio (S. Agata), 98166 Messina, Italy

(Received 6 October 2015; revised 17 June 2016; accepted 30 September 2016; first published online 4 November 2016)

Numerical simulations of wall-bounded acceleration-skewed oscillatory flows are here presented. The relevance of this type of boundary layer arises in connection with coastal hydrodynamics and sediment transport, as it is generated at the bottom of sea waves in shallow water. Because of the acceleration skewness, the bed shear stress during the onshore half-cycle is larger than in the offshore half-cycle. The asymmetry in the bed shear stress increases with increasing acceleration skewness, while an increase of the Reynolds number from the laminar regime causes the asymmetry first to decrease and then increase. Low- and high-speed streaks of fluid elongated in the streamwise direction emerge near the wall, shortly after the beginning of each half-cycle, at a phase that depends on the flow parameters. Such flow structures strengthen during the first part of the accelerating phase, without causing a significant deviation of the streamwise wall shear stress from the laminar values. Before the occurrence of the peak of the free stream velocity, the low-speed streaks break down into small turbulent structures causing a large increase in wall shear stress. The ratio of the root-mean-square (r.m.s.) of the fluctuations to the mean value (relative intensity) of the wall shear stress is approximately 0.4 throughout a relatively wide interval of the flow cycle that begins when breaking down of the streaks has occurred in the entire fluid domain. The acceleration skewness and the Reynolds number determine the phase at which this time interval begins. Both the skewness and the flatness coefficients of the streamwise wall shear stress are large when elongated streaks are present, while values of approximately 1.1 and 5.4 respectively occur just after breaking has occurred. The trend of both the relative intensity and the flatness of the spanwise wall shear stress are qualitatively similar to those of the wall shear in the streamwise direction. As a result of the acceleration skewness, the period-averaged Reynolds stress does not vanish. Consequently, an offshore directed steady streaming is generated which persists into the irrotational region.

Key words: coastal engineering, surface gravity waves, turbulent boundary layers

---

† Email address for correspondence: pscandu@dica.unict.it

1. Introduction

Oscillating flows are relevant in several hydrodynamic phenomena of both engineering and environmental interest such as unsteady flows in pipes and water wave propagation. Most of the knowledge about fundamental physical aspects of oscillating boundary layers comes from studies on the sinusoidally oscillating boundary layer, which is also known as the Stokes layer. Systematic experiments on the Stokes layer were carried out by Jensen, Sumer & Fredsøe (1989) covering a wide range of Reynolds numbers. Transition to turbulence was detected at $Re \approx 10^5$, where Re is the Reynolds number based on the peak of the free stream velocity and on half the amplitude of fluid displacement in the irrotational region. Later, Vittori & Verzicco (1998) carried out a numerical study in order to understand how transition to turbulence in a Stokes layer is affected by wall imperfections. Flow perturbations due to wall imperfections has also been examined by Scandura (2013), who showed that important deviations from the laminar Stokes solution are generated in the boundary layer when imperfections characterized by a slope as low as 10^{-4} are added to an originally flat wall. The largest flow destabilization is provided by imperfections with a dimensionless wavelength L/δ equal to approximately $2\pi/0.36$, where $\delta = \sqrt{2\nu/\sigma}$ is the conventional thickness of the oscillating boundary layer, ν is the kinematic viscosity and σ is the angular frequency of fluid oscillations. This finding shows why two-dimensional instabilities are detected in several experiments even at sub-critical Reynolds numbers (Carstensen, Sumer & Fredsøe 2010). Costamagna, Vittori & Blondeaux (2003) studied vortex structures in a Stokes layer and concluded that the streak instability is the most important mechanism that sustains turbulence. Large eddy simulations of the Stokes layer were carried out by Salon, Armenio & Crise (2007) who reproduced an experimental test of Jensen *et al.* (1989). One of the main conclusions of this work is that there are intervals of the flow cycle where turbulence shows features similar to those of a steady wall-bounded flow. The same test of Jensen *et al.* (1989) was also simulated by Pedocchi, Cantero & Garcia (2011), by means of direct numerical simulation, focusing primarily on the turbulent kinetic energy balance. The effect of the initial condition on the transition to turbulence in a Stokes layer has been studied by Ozdemir, Hsu & Balachandar (2014), who reported that sustainable transition depends on the Reynolds number but also on the initial condition.

Near the coast, the characteristics of the oscillating boundary layer at the bottom of sea waves mostly depend on the wave shape, which undergoes important changes during wave propagation from deep to shallow waters. In deep waters the wave shape is close to a sinusoid, consequently a Stokes boundary layer should be produced at the bottom, however, no motion is induced near the sea bed because of the large depth. At intermediate depths, because of nonlinearities, the crests become narrow and sharp and the through broad and flat, thus giving rise to skewed waves. Such a wave shape induces a velocity skewness in the boundary layer as the magnitude of the onshore velocity under the crest is larger than that of the offshore velocity under the trough. When the waves reach the shallow water region they also become asymmetric, with a steep front and a gently sloping rear face (Elgar, Guza & Freilich 1988), thereby acquiring a sawtooth shape. Under asymmetric waves the magnitude of the near bed onshore acceleration is larger than that of the offshore acceleration, therefore the time development of the velocity is characterized by an acceleration skewness. In the field, wave skewness and asymmetry coexist near the coast and have a strong impact on both the hydrodynamics and the sediment transport. In this context, several studies have been carried out to understand the physical processes that occur in the bottom boundary layer, most often by considering wave skewness and asymmetry in isolation from each other, in order to simplify the framework and facilitate the interpretation of the results. Some of these studies were mainly focused on sediment transport processes, while others were more focused on the hydrodynamics.

Experiments on velocity-skewed oscillatory flows on a sandy bed were carried out by Ribberink & Al-Salem (1995) in an oscillatory water tunnel. The authors reported that the net sediment transport during the cycle is onshore directed although a net-wave-averaged horizontal velocity develops having opposite direction to that of wave propagation. The effect of velocity skewness has been introduced into a mathematical model of the turbulent wave boundary layer by Trowbridge & Madsen (1984), who showed that for long waves in shallow waters an offshore current occurs. Both Dibajnia & Watanabe (1998) and O'Donoghue & Wright (2004) found that velocity skewness increases the transport of sediment towards the coast, but they also found that it may give rise to an offshore transport of fine sediments. Holmedal & Myrhaugh (2006) and Fuhrman, Fredsøe & Sumer (2009) reproduced the experimental results of Ribberink & Al-Salem (1995) by means of a numerical model. Insights into the physical mechanism responsible for steady streaming in a velocity-skewed oscillatory flow has also been provided by Scandura (2007). The reliability of the most employed turbulent closure models in predicting the features of a velocity-skewed oscillatory flow has been analysed by Cavallaro, Scandura & Foti (2011). In this study, a ranking of the models was provided but it was also noted that their performance mostly depends on the flow quantity under investigation. Blondeaux *et al.* (2012) developed a mathematical model to reproduce the hydrodynamics and the sediment transport within the bottom boundary layer under velocity-skewed waves. According to their model, sediment transport is onshore directed while the steady streaming can be onshore or offshore directed, depending on the flow parameters.

The first to recognize that acceleration skewness has an important role in driving onshore sediment transport was Madsen (1974). The author reported that the pressure gradient induced by the wave passage may be of sufficient magnitude to induce bed instability. Several years later, King (1990) carried out experiments in a U-tube which proved that acceleration skewness gives rise to onshore sediment transport. Drake & Calantoni (2001) and Calantoni & Puleo (2006) developed and applied a three-dimensional discrete particle model to describe sheet flow sediment transport under acceleration-skewed waves. Nielsen & Callaghan (2003) developed a method to predict the sediment transport rates accounting both for acceleration skewness and boundary layer streaming. Hsu & Hanes (2004) applied a two-phase model to examine the effect of wave shape on sheet flow sediment transport. Their results indicated that both asymmetric and skewed waves provide onshore sediment transport. Laboratory experiments in a U-tube were performed by Watanabe & Sato (2004), who also confirmed that the wave-averaged sediment transport does not vanish under an acceleration-skewed oscillatory flow. More recently, experiments have been carried out by van der A *et al.* (2010), Silva *et al.* (2011) and Dong, Sato & Liu (2013) who showed that the net sediment transport has the direction of the largest acceleration and that the phase lag of the bed shear stress plays an important role in determining the direction and the magnitude of the sediment flux. Abreu *et al.* (2013) developed a new parametrization for the bed shear stress in oscillatory flows by introducing an index of skewness and a waveform parameter.

A detailed experimental study on the hydrodynamics of acceleration-skewed oscillatory boundary layers on a rough wall has been carried out by van der A *et al.* (2011). This study clearly shows that the acceleration skewness induces an asymmetry of the wall shear stress between the two half-cycles. The existence of a steady streaming having the opposite direction to that of the largest acceleration is also detected in their study. In the field, the mass transport generated outside the bottom boundary layer may also have an effect on the transport of fine sediments, which can be easily brought far away from the bottom (Scandura & Foti 2011; Scandura, Foti & Faraci 2012).

Within the context described above, the present paper analyses results of direct numerical simulations of wall-bounded acceleration-skewed oscillatory flows. The range of Reynolds numbers partially overlaps with that of van der A *et al.* (2011), but unlike the previous investigation, the bottom is assumed smooth. The reason for limiting the present study to the case of a smooth wall is due to the formidable computational task posed by a direct numerical simulation on a real rough wall. However, we feel that the present study provides interesting insights which might be of help to formulate models of sediment transport under sea waves; moreover it provides a good basis for advancing the study to the case of rough a wall.

The paper is organized as follows. In § 2 the problem is formulated and the numerical approach is briefly described along with some tests on the numerical code. In § 3.1 the ensemble average of the wall shear stress and of the velocity profiles are discussed. In § 3.2 the characteristics of the turbulent structures in the near-wall region are analysed. The turbulent kinetic energy and the Reynolds stress are analysed in § 3.3. Section 3.4 is mainly devoted to the analysis of the wall shear stress statistics. Finally, conclusions are drawn in § 4.

2. Formulation of the problem and numerical approach

We consider a prototype of the oscillatory flow induced by sawtooth waves near a flat bottom. Hereinafter an asterisk denotes a dimensional variable. As a reference a Cartesian coordinate system with the x^* and z^* axes lying on the bottom, the x^* axis pointing onshore and the y^* axis pointing outward from the bottom is introduced. The velocity components along the x^*, y^* and z^* axes are denoted as u^*, v^* and w^* respectively. When writing the governing equations, for convenience the axes of the reference system and the velocity components are denoted as (x_1^*, x_2^*, x_3^*) and (u_1^*, u_2^*, u_3^*) respectively. We assume that at the outer edge of the boundary layer the fluid oscillates along the x^* direction as (van der A *et al.* 2011):

$$u^* = u^*_{max}\alpha \sum_{n=1}^{N} \frac{(2\xi - 1)^{n-1}}{n} \sin(n\sigma^* t^*), \tag{2.1}$$

where t^* is the time, $\sigma^* = 2\pi/T^*$ is the angular frequency, T^* is the period, α is a coefficient such that the maximum of u^* in (2.1) is equal to u^*_{max} and ξ is a parameter whose value is chosen as specified below. The degree of acceleration skewness of the free stream velocity is measured by the acceleration skewness parameter $\beta = \dot{u}^*_{t^*=0}/(\dot{u}^*_{t^*=0} - \dot{u}^*_{t^*=T^*/2})$, where a dot denotes a time derivative evaluated at $t^* = 0$ or at $t^* = T^*/2$. In general $\dot{u}^*_{t^*=0}$ is equal to the maximum acceleration during the cycle, while $\dot{u}^*_{t^*=T^*/2}$ approximates the minimum of the acceleration only when N is large. Therefore, for sufficiently large N, it is possible to write $\beta = \dot{u}^*_{max}/(\dot{u}^*_{max} - \dot{u}^*_{min})$. When $N = 1$ we get $\beta = 0.5$ for any value of ξ. For $N > 1$, $\xi = \beta$ when N is even, while $\xi = (\dot{u}^*_{t^*=0} - \alpha\sigma^* u^*_{max})/(\dot{u}^*_{t^*=0} + \dot{u}^*_{t^*=T^*/2})$ for odd values of N. For large N, ξ tends to β without distinction between even and odd values of N. Here N is chosen to be 20, as it is sufficiently large to assume that $\xi = \beta = \dot{u}^*_{max}/(\dot{u}^*_{max} - \dot{u}^*_{min})$.

At the outer edge of the boundary layer the pressure gradient consistent with the free stream velocity given by (2.1) reads:

$$\frac{\partial P^*}{\partial x^*} = -\varrho^* u^*_{max} \alpha \sigma^* \sum_{n=1}^{20} (2\beta - 1)^{n-1} \cos(n\sigma^* t^*), \tag{2.2}$$

where ϱ^* is the fluid density and $\partial P^*/\partial x^*$ is the pressure gradient that drives the flow. The following dimensionless variables are introduced:

$$t = t^*\sigma^*, \quad (x, y, z) = \frac{x^*, y^*, z^*}{\delta^*}, \quad (u, v, w) = \frac{u^*, v^*, w^*}{u^*_{max}}, \quad p = \frac{p^*}{\varrho^* u^{*2}_{max}}, \tag{2.3a–d}$$

where p^* is the pressure due to the flow in the boundary layer, δ^* is the thickness of the laminar boundary layer defined as $\delta^* = \sqrt{2\nu^*/\sigma^*}$ and ν^* is the kinematic viscosity of the fluid. The bottom shear stresses along the x and z directions are denoted as τ_x and τ_z respectively and they are made dimensionless in the same manner as the pressure.

The continuity and the Navier–Stokes equations in dimensionless form can be written as follows:

$$\frac{\partial u_j}{\partial x_j} = 0, \tag{2.4}$$

$$\frac{\partial u_i}{\partial t} + \frac{R_\delta}{2} \frac{\partial u_i u_j}{\partial x_j} = -\delta_{1,i} \frac{R_\delta}{2} \frac{\partial P}{\partial x_1} - \frac{R_\delta}{2} \frac{\partial p}{\partial x_i} + \frac{1}{2} \frac{\partial^2 u_i}{\partial x_j \partial x_j}, \tag{2.5}$$

where $\delta_{1,i}$ is the Kronecker delta and repeated subscripts denote a summation with j ranging from 1 to 3. The dimensionless pressure gradient $\partial P/\partial x_1$, that appears on the right-hand side of the Navier–Stokes equation, can be written as follows (see (2.2)):

$$\frac{\partial P}{\partial x_1} = -\frac{2\alpha}{R_\delta} \sum_{n=1}^{20} (2\beta - 1)^{n-1} \cos(nt). \tag{2.6}$$

Equations (2.4)–(2.6) show that the flow is characterized by two dimensionless parameters, i.e. the acceleration skewness β and the Reynolds number $R_\delta = u^*_{max}\delta^*/\nu^*$. It is worth pointing out that the Reynolds number $Re = u^{*2}_{max}/(\sigma^*\nu^*)$ can be introduced in place of R_δ since the two Reynolds numbers are linked by means of the relation $Re = R^2_\delta/2$. In the case of a laminar flow, the integration of (2.4), (2.5), with $\partial P/\partial x_1$ given by (2.6), provides the following expression for the streamwise velocity:

$$u = \alpha \sum_{n=1}^{N=20} \frac{(2\beta - 1)^{n-1}}{n} [\sin(nt) - e^{-\sqrt{n}y} \sin(nt - \sqrt{n}y)]. \tag{2.7}$$

The flow considered in this study is turbulent during most of the wave cycle, hence the Navier–Stokes equations must be integrated numerically. The employed numerical approach is based on centred second-order finite differences on a staggered grid. The time advancement employs a fraction-step method which is a variant of that described by Kim & Moin (1985). In order to compute the intermediate non-solenoidal velocity field, the viscous terms are discretized by the Crank–Nicholson scheme and the convective terms by a third-order Runge–Kutta scheme. The Poisson equation for the pressure, obtained by imposing mass conservation, is solved by applying the Fourier transform along the x and z directions. The domain of integration has sizes L_x, L_y and L_z in the x, y and z directions respectively. On the wall ($y=0$) the no-slip condition is imposed $(u, v, w)=(0, 0, 0)$, while at the top of the computational domain ($y=L_y$) a free shear stress condition is introduced $(\partial(u, w)/\partial y, v)=(0, 0, 0)$. Finally, the flow is assumed to be homogeneous along the directions parallel to the wall, therefore, periodic boundary conditions are introduced along the x and the z axes. The grid spacing is uniform along the x and z directions, while along the y direction the grid is clustered near the wall where large gradients exist. The distribution of the grid points along the y direction is computed by means of a hyperbolic tangent function.

Six cases of acceleration-skewed oscillatory flow obtained by combining two values of the Reynolds number ($R_\delta = 1100, 1414$) with three values of the β parameter ($\beta = 0.60, 0.75, 0.85$) are here considered. In addition, 10 simulations were carried out for $\beta = 0.75$ and Reynolds numbers ranging between the laminar regime and $R_\delta = 1100$ in order to gain insights about the trend of the wall shear stress asymmetry. Details about these simulations are given in § 3.1.

The ensemble average is denoted by enclosing the symbol of the quantity between brackets $\langle\cdot\rangle$, with the exception of τ_x for which the symbol τ_0 is used. By exploiting the statistical homogeneity of the flow in the (x, z) planes, the ensemble average is evaluated by performing spatial averages along the two periodic directions, followed by a phase average over 14 cycles, with the exception of $\beta=0.75$ and $R_\delta=1100$ and $R_\delta = 1414$, for which 33 and 24 cycles respectively were used for phase averaging. The larger amount of cycles for the previous simulations, allowed us to verify that 14 cycles were sufficient to get reliable ensemble averages. In the previous study by Salon *et al.* (2007), 14 cycles were also used for phase averaging.

The initial condition of the simulation was given by the laminar velocity profile at $t=0$ (see (2.7)). In order to trigger transition to turbulence, wall imperfections of small amplitude, similar to those described in Scandura (2007), were introduced. Generally, transition to turbulence was achieved within the first two cycles. After transition occurred, the wall imperfections were removed and the simulation was continued on a perfectly smooth wall. This procedure, involving wall imperfections to initiate turbulence, was adopted only for the first numerical simulation carried out for a given value of β, which in all cases was for $R_\delta = 1100$. For the other simulations the flow field provided by a previous simulation has been used as initial condition. This approach was never applied by using a flow field characterized by a different value of β, since it would cause a very slow convergence towards the flow representative of the β value under consideration. For all the cases, the flow was independent on the initial condition after 10 cycles from the beginning of the simulation, hence the first 10 cycles have not been included in the computation of the ensemble average.

The dimensions of the computational domain L_x and L_z were chosen to be 50 and 25 respectively for all the computations, while the dimension L_y was set equal to 35 for $R_\delta = 1100$ and 40 for $R_\delta = 1414$. The adequacy of these dimensions has been controlled by ensuring that the spatial autocorrelation function of the velocity components decays within half of the computational domain. The dimensions of the numerical grid n_x, n_y and n_z along the x, y and z directions respectively, were chosen to be $(n_x, n_y)=(200, 180)$ for all the computations, while $n_z=240$ for $R_\delta=1100$ and $n_z=320$ for $R_\delta=1414$. The increase of n_z is necessary since the near-wall turbulent structures (see § 3.2) are elongated in the streamwise direction and become thinner when the Reynolds number increases. When R_δ increases, a grid refinement is also required in the wall-normal direction, within the boundary layer, which in this study was obtained by a slight increase of the grid clustering near the wall.

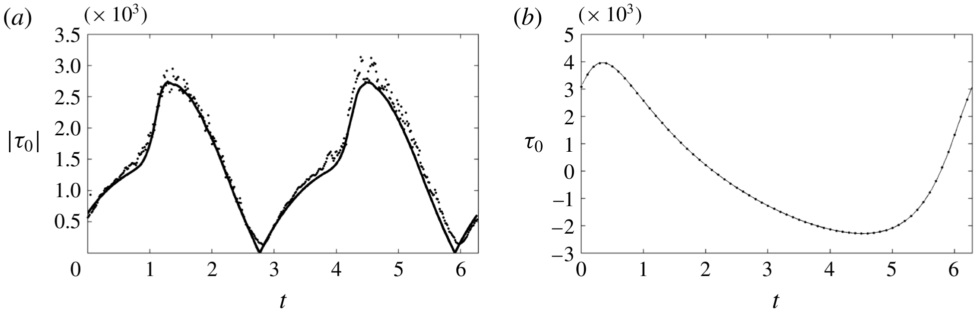

FIGURE 1. Comparison between the wall shear stress measured in test 7 of Jensen *et al.* (1989) (markers) and that computed by means of the present numerical code (continuous line) for $\beta = 0.5$ and $R_\delta = 1120$ (*a*); comparison between the wall shear stress computed by means of (2.7) (continuous line) and the wall shear stress computed by means of the present numerical approach (markers) for $\beta = 0.75$ and $R_\delta = 500$ (*b*).

In terms of spatial resolution, the most demanding numerical simulation is that characterized by $R_\delta = 1414$ and $\beta = 0.85$. At the phase of the peak of the wall shear stress, the minimum wall-normal grid spacing in wall units is $\Delta y^+ = 1$, while along the x and z direction the resolution is $\Delta x^+ = 19.8$ and $\Delta z^+ = 6.19$. In terms of Kolmogorov length scale, η, evaluated by considering the peak of the turbulent kinetic energy dissipation at the wall, the grid spacings for this simulation take the following values: $\Delta x_\eta = 13.1$, $\Delta y_\eta = 0.7$ and $\Delta z_\eta = 4.1$. The best spatial resolution is achieved for the flow characterized by $R_\delta = 1100$ and $\beta = 0.60$, for which the grid spacing in wall units is $\Delta x^+ = 14.70$, $\Delta y^+ = 0.78$, $\Delta z^+ = 6.12$ and in terms of Kolmogorov length scale is $\Delta x_\eta = 10.2$, $\Delta y_\eta = 0.54$, $\Delta z_\eta = 4.25$. As pointed out by Moin & Mahesh (1998), in a direct numerical simulation it is not necessary that the smallest resolved spatial scale is equal to η, values of order 10 are also acceptable. The adequacy of the grid resolution for $R_\delta = 1414$ is highlighted by the decay of the energy spectra at high wavenumbers shown in figure 16. Indeed, it can be observed that the energy at high wavenumbers is approximately five orders of magnitude smaller than that at low wavenumbers.

In order to demonstrate the correctness of the numerical code, test number 7 of Jensen *et al.* (1989) ($\beta = 0.5$, $R_\delta = 1120$) has been simulated and results of the time development of the ensemble-averaged wall shear stress are compared with the experimental measurements in figure 1(*a*). This test has been simulated using the same computational domain and the same numerical grid adopted for $R_\delta = 1100$ as the spatial resolution requirements of the two cases are similar. Indeed, in terms of wall units the resolution is: $\Delta x^+ = 14.8$, $\Delta y^+ = 0.79$, $\Delta z^+ = 6.2$, while in terms of Kolmogorov length scale it is: $\Delta x_\eta = 9.95$, $\Delta y_\eta = 0.53$, $\Delta z_\eta = 4.14$. The computation of the ensemble average is based on 14 cycles. Figure 1(*a*) shows that there is a fairly good agreement between the experimental measurements and the numerical results. The slight discrepancies that emerge during the second half-cycle are due to the small asymmetry of the flow produced by the U-tube employed by Jensen *et al.* (1989). The result in figure 1(*a*) supports the adequacy of both the numerical grid and of the number of cycles used to compute the ensemble average. Figure 1(*b*) shows a comparison between the wall shear stress in acceleration-skewed oscillatory flow, provided by the analytical solution given by (2.7), and the wall shear stress computed by means of the numerical code. It can be observed that the two approaches provide indistinguishable results one from each other.

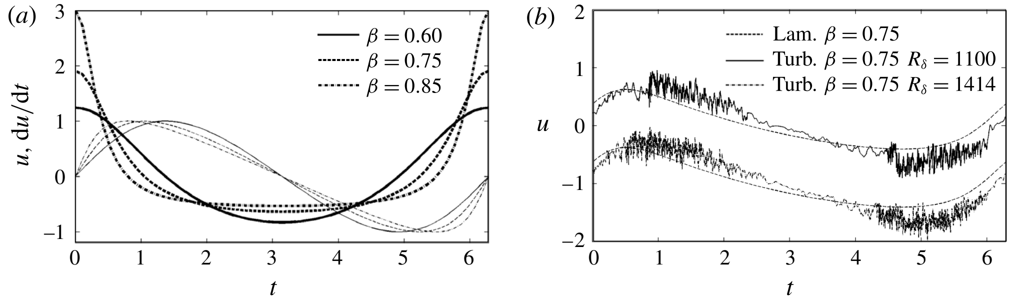

FIGURE 2. (a) Free stream velocity and acceleration for three different values of β. The maximum dimensionless velocity has been fixed to 1 in all the cases; thin lines: velocity; thick lines: acceleration; (b) time development of the streamwise velocity component u, in a position in the $y = 0.42$ plane. For $R_\delta = 1414$ the trends are offset by −1.

3. Numerical results and discussion

In figure 2(a) both the free stream velocity and the acceleration determined by (2.7) are shown. The positive and the negative peaks of the velocity are equal to each other while the positive peak of the acceleration is larger than the negative one. The phases t_+ and t_-, at which the positive and the negative peaks of the free stream velocity occur respectively, take the following values: $t_+ = 1.38$ and $t_- = 4.9$ for $\beta = 0.6$; $t_+ = 1.04$ and $t_- = 5.24$ for $\beta = 0.75$; $t_+ = 0.785$ and $t_- = 5.5$ for $\beta = 0.85$. It can be noted that when β increases the phase of the positive peak of the velocity shifts back, while the phase of the negative peak shifts forward. In figure 2(b) a realization of the streamwise velocity component during a period, in the $y = 0.42$ plane, is shown for $\beta = 0.75$ and for the two Reynolds numbers here considered along with the velocity that would occur if the flow were laminar. During the first stage of the accelerating phase the velocity shows only small fluctuations. Large turbulent fluctuations suddenly emerge before the end of the accelerating phase and persist during a large part of the deceleration. Turbulence almost disappears in the vicinity of flow reversal but it suddenly emerges again before the end of the accelerating phase of the negative half-cycle. During the following decelerating phase the turbulence decays again and the flow recovers a laminar-like behaviour. An increase of R_δ anticipates the onset of the turbulence, while, as regards the persistency of the turbulence up to the vicinity of the flow reversal, the increase of the Reynolds number does not have a similar important effect. The intermittent appearance of turbulence is typical of oscillatory flows, it has been previously detected both in Stokes boundary layers (Jensen *et al.* 1989; Vittori & Verzicco 1998; Costamagna *et al.* 2003; Salon *et al.* 2007) and in wall-bounded velocity-skewed oscillatory flows (Scandura 2007; Cavallaro *et al.* 2011).

3.1. *Ensemble-averaged wall shear stress and velocity profiles*

In figure 3(a,b) the time development of the ensemble-averaged wall shear stress τ_0 is shown for both turbulent and laminar flow. During the first stage of the positive half-cycle, because of the large flow acceleration, the vorticity produced at the wall has a short time to spread, leading to a large near-wall velocity gradient (Nielsen & Callaghan 2003). Consequently, the positive peak of the wall shear stress is larger than the negative one, as shown in figure 3(a,b). The asymmetry of the wall shear stress can be evaluated through the asymmetry parameter A_{τ_0} defined as:

$$A_{\tau_0} = \frac{\tau_{0max} + \tau_{0min}}{\tau_{0max}}, \qquad (3.1)$$

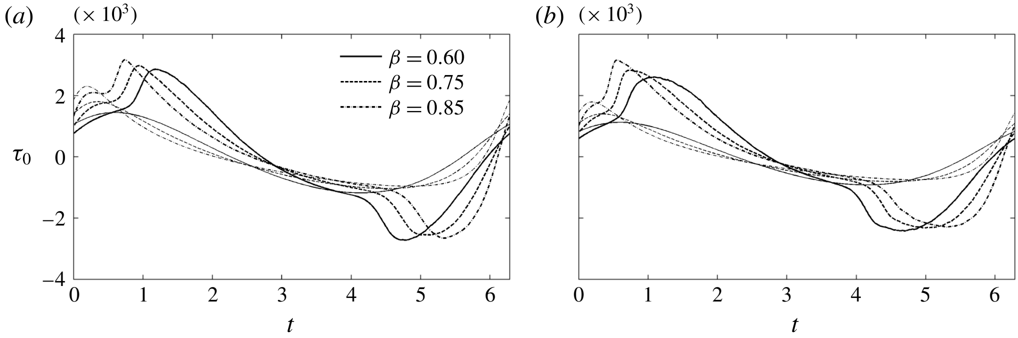

FIGURE 3. Time development of the ensemble-averaged wall shear stress during a cycle. (*a*) $R_\delta = 1100$, (*b*) $R_\delta = 1414$. Thin lines: laminar flow; thick lines: turbulent flow.

R_δ	β					
	0.60	0.75	0.85	0.60	0.75	0.85
	A_{τ_0}			Γ_{τ_0}		
1100	0.045	0.14	0.16	0.06	0.147	0.231
1414	0.070	0.177	0.272	0.069	0.176	0.30
	Asymmetry in laminar flow					
	0.183	0.423	0.581	0.216	0.595	0.969

TABLE 1. Asymmetry parameters A_{τ_0} and Γ_{τ_0} of the bottom shear stress.

where τ_{0max} and τ_{0min} are the maximum and the minimum values of the wall shear stress during the cycle. Another measure for the asymmetry is given by Γ_{τ_0} which is defined as follows:

$$\Gamma_{\tau_0} = \frac{M_3}{\sigma_{\tau_0}^3}, \quad \text{where } M_3 = \frac{1}{2\pi}\int_0^{2\pi} \tau_0^3 \, \mathrm{d}t \text{ and } \sigma_{\tau_0} = \sqrt{\frac{1}{2\pi}\int_0^{2\pi} \tau_0^2 \, \mathrm{d}t}. \tag{3.2}$$

Table 1 shows that A_{τ_0} and Γ_{τ_0} have similar trends as functions of the flow parameters, even though there are quantitative differences between themselves. It can be observed that the asymmetry increases both with acceleration skewness and Reynolds number, however, in laminar flow it is larger than in turbulent flow. This finding shows that a Reynolds number threshold, below which the asymmetry decreases with R_δ and above which it increases, exists for Reynolds number smaller than those considered in table 1, thus suggesting that the asymmetry has a minimum. Following these results, the effect of the Reynolds number on the asymmetry of the wall shear stress in the range between the laminar regime and $R_\delta = 1100$ was investigated. A series of 10 numerical simulations was therefore performed for $R_\delta < 1100$ and $\beta = 0.75$ in order to describe the trend of the asymmetry. For all these simulations the same computational domain and grid size adopted for $R_\delta = 1100$ were employed. The ensemble average was computed by phase averaging over 35 cycles.

In figure 4(*a*), where the trends of A_{τ_0} and Γ_{τ_0} are shown, it can be observed that when the Reynolds number decreases below 1100, A_{τ_0} decreases and attains the minimum at approximately $R_\delta = 925$. On the other hand Γ_{τ_0} does not show important

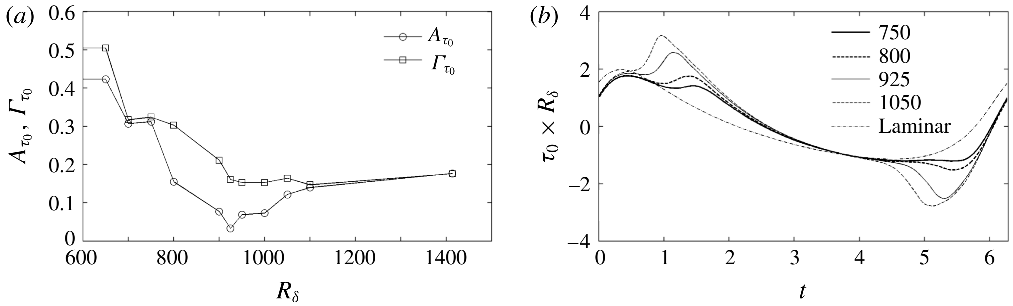

FIGURE 4. Asymmetry parameters A_{τ_0} and Γ_{τ_0} as functions of the Reynolds number (*a*); ensemble-averaged wall shear stress (*b*). $\beta = 0.75$.

variations as long as R_δ is larger than approximately 900. A decrease of R_δ below 900 causes an increase of both A_{τ_0} and Γ_{τ_0}. For $R_\delta = 650$ the flow is found to be laminar, therefore the asymmetries take the values reported in table 1 for laminar flow. In order to illustrate why the asymmetry in turbulent flow may be much smaller than in laminar flow, figure 4(*b*) shows the trend of the wall shear stress for Reynolds numbers 750, 800, 925 and 1050 along with the laminar wall shear stress. The quantity $\tau_0 \times R_\delta$ in figure 4(*b*) is the wall shear stress scaled by $\varrho^* \nu^* u^*_{max}/\delta^*$, which use turns out to be advantageous since all the curves in laminar flow collapse on each other. At $R_\delta = 750$ the flow is already in the intermittently turbulent regime, hence, turbulence develops during the decelerating phase of the positive half-cycle, causing the appearance of a secondary peak in the wall shear stress. Turbulence also develops during the decelerating phase of the negative half-cycle, hence a small secondary peak also appears at approximately $t = 5.5$. These peaks do not exceed the main ones, therefore the asymmetry A_{τ_0} still depends on the main ones. For such a low Reynolds number the main peaks of τ_0 are slightly smaller than in laminar flow and to a greater extent this occurs in the positive half-cycle, therefore a decrease of A_{τ_0} with respect to the laminar flow is observed. When the Reynolds number increases up to 800, the secondary peak of the first half-cycle becomes close to the main one but in the negative half-cycle it exceeds the main one, therefore a decrease of A_{τ_0} with respect to $R_\delta = 750$ occurs. The smaller decrease of Γ_{τ_0} with respect to A_{τ_0} is due to the increase of the second peak in the positive half-cycle which provides a positive contribution to Γ_{τ_0} but it does not affect A_{τ_0}. A further increase of the Reynolds number causes an increase of the secondary peaks which finally become the only one of each half-cycle. In particular, for $R_\delta = 925$ a large decrease of the asymmetry with respect to that in laminar regime is detected. The proximity of the two peaks, combined with the circumstance that τ_{0max} in turbulent flow is substantially larger than in laminar flow, explains such a result (see (3.1)).

When R_δ takes larger values, the onset of turbulence shifts back in time during the cycle. Hence, in the positive half-cycle the peak of the wall shear stress occurs when the laminar wall shear stress is larger, thus causing an increase of τ_{0max} with respect to lower R_δ. In the negative half-cycle the trend of the laminar wall shear stress is rather constant near the peak, therefore the magnitude of τ_{0min} increases to a lesser extent with respect to τ_{0max}. Overall, these effects induce an increase of the asymmetry when R_δ increases beyond a value of approximately 925. It is much more difficult to explain the trend of Γ_{τ_0} especially in the range $R_\delta = 900$–1100, where important qualitative differences with respect to A_{τ_0} are observed. Such differences are, however, easy to

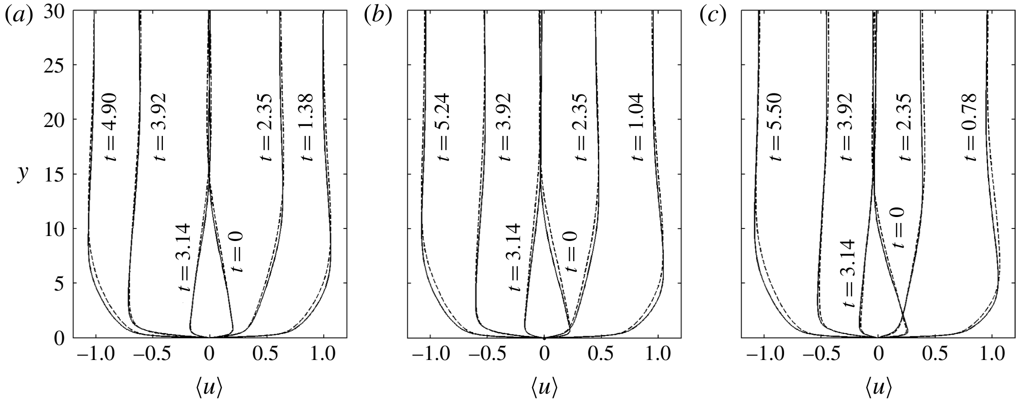

FIGURE 5. Ensemble-averaged velocity profiles at different phases during the period (*a*) $\beta = 0.6$, (*b*) $\beta = 0.75$, (*c*) $\beta = 0.85$. Continuous line: $R_\delta = 1100$; dashed line: $R_\delta = 1414$.

R_δ	β					
	0.60		0.75		0.85	
	y_{max}	y_{min}	y_{max}	y_{min}	y_{max}	y_{min}
1100	7.03	9.03	5.95	9.67	4.59	10.39
1414	9.40	10.31	7.87	12.36	6.03	12.86
	Laminar flow					
	2.2	2.5	1.88	2.8	1.64	3.04

TABLE 2. Distances from the wall y_{max} and y_{min} of the maximum and of the minimum velocity respectively during the cycle. According to the present scaling, in laminar flow y_{max} and y_{min} do not depend on the Reynolds number.

accept as A_{τ_0} only depends on the peaks of the wall shear stress while Γ_{τ_0} depends on the overall trend. The increase of the asymmetry with R_δ qualitatively agrees with the experimental findings of van der A *et al.* (2011).

In figure 5(*a*,*b*,*c*) the ensemble-averaged velocity profiles are shown for $\beta = 0.60$, 0.75 and 0.85 respectively. In these figures the velocity profiles are plotted at the phases $t = 0$, 2.35, 3.14, 3.92 and at two additional phases depending on the β parameter and characterized by the maximum and the minimum value respectively of the free stream velocity during the cycle. Comparing figure 5(*a*–*c*) we observe that the distance y_{max} from the wall of the position of maximum velocity decreases with β as a result of the increased acceleration. On the other hand, the distance y_{min} of the position of minimum velocity increases with β. Such an increase occurs because in the negative half-cycle the vorticity has a longer time to spread far from the wall when β increases (Nielsen & Callaghan 2003). Table 2 shows the distances y_{max} and y_{min}, which can be assumed as a measure of the thickness of the boundary layer. It can be noted that as the Reynolds number increases both y_{max} and y_{min} increase. This result is somewhat expected as generally turbulent diffusivity increases with R_δ. The data in table 2 also allow for assessment of the thickness of the boundary layer in turbulent flow and to compare it with that in laminar flow.

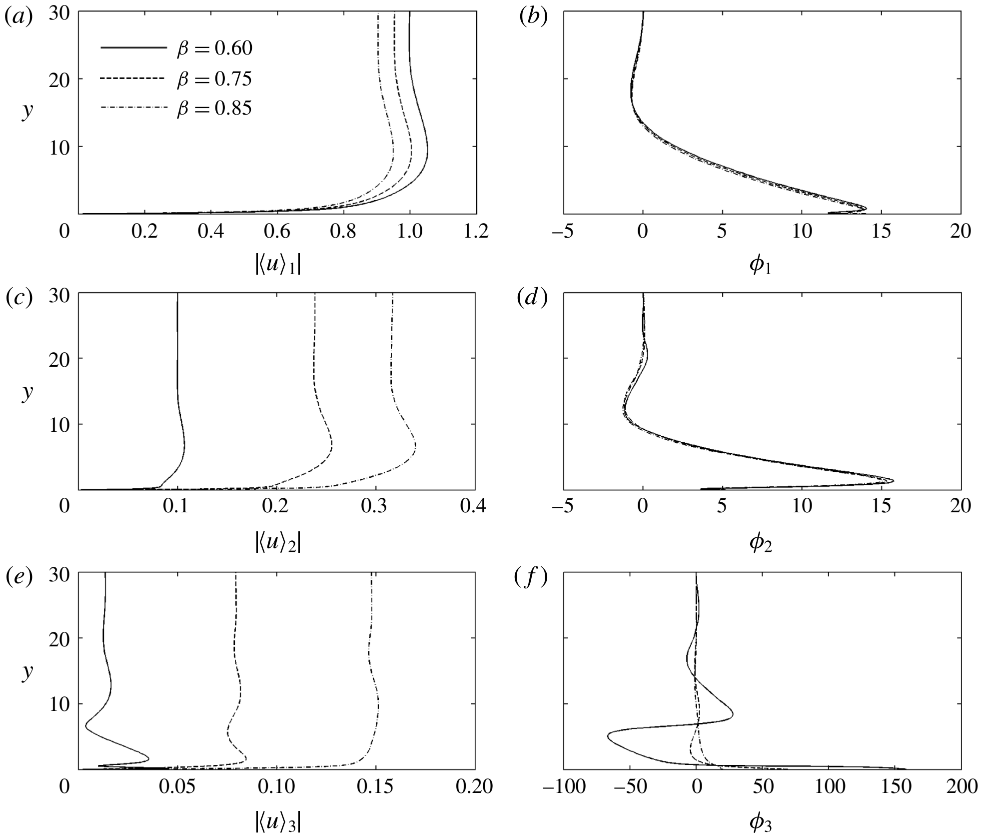

FIGURE 6. Amplitudes $|\langle u\rangle_1|$, $|\langle u\rangle_2|$ and $|\langle u\rangle_3|$ (*a*,*c*,*e*) and phases ϕ_1, ϕ_2 and ϕ_3 (*b*,*d*,*f*) of the first three harmonic components of the ensemble-averaged velocity profiles for $R_\delta = 1100$.

In figure 6 the amplitude $|\langle u\rangle_n|$ and the phase ϕ_n of the first three harmonic components of the ensemble-averaged velocity are plotted. Far from the wall, where the flow is irrotational, the amplitudes are given by (2.1). Within the boundary layer the amplitudes vary and vanish at the bottom where the no-slip condition is satisfied. A comparison among the first components in figure 6(*a*), shows that the smaller is β the larger is the component. For the second and the third harmonic components (figure 6*c*,*e*), the comparison shows the opposite. The trends along the y-axis of the first and of the second component are qualitatively similar to each other both in terms of amplitudes and phases for all the considered values of β (figure 6*a*–*d*). On the other hand, the third component shown in figure 6(*e*) exhibits large fluctuations near the bottom which increase as β decreases. Analogous fluctuations can also be observed in figure 6(*f*) as regards the phase. Present results have several points in common with those reported in figure 5 of van der A *et al.* (2011), including the large oscillations of the profile of the harmonic components for low values of β. Analogous results are observed for $R_\delta = 1414$.

In figure 7 the ensemble-averaged velocity profiles in semi-log plot are shown at 16 phases for $R_\delta = 1100$. Note that the logarithm of the absolute value of the velocity is plotted, therefore near flow reversal, a discontinuity in the first derivative may appear

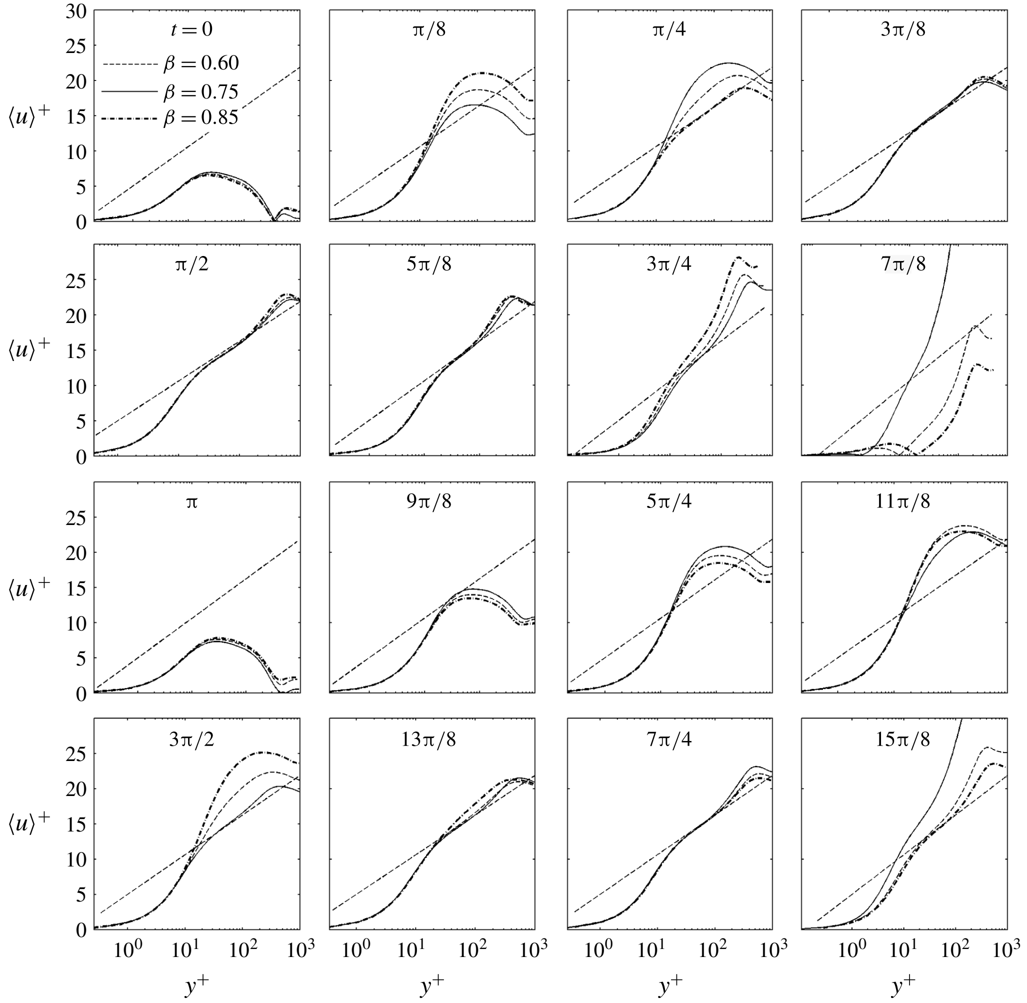

FIGURE 7. Ensemble-averaged velocity profiles in semi-log plot during the period for $R_\delta = 1100$. Thin dashed line: $\langle u\rangle^+ = \log(y^+)/0.41 + 5$.

such as at $t = 0$ and $t = 7\pi/8$. In this figure the length is expressed in wall units ($y^+ = yR_\delta\sqrt{\tau_0}$) while $\langle u\rangle^+$ is the ensemble-averaged velocity made dimensionless by means of the instantaneous friction velocity ($\langle u\rangle^+ = \langle u\rangle/\sqrt{\tau_0}$). As shown in figure 7, logarithmic layers are not detected in the early stage of the accelerating phase. A logarithmic layer emerges between $\pi/8$ and $\pi/4$ for $\beta = 0.85$ and between $\pi/4$ and $3\pi/8$ for $\beta = 0.75$ and $\beta = 0.6$. During the decelerating phase the logarithmic velocity profile persists up to $5\pi/8$ and completely disappears near flow reversal. In the negative half-cycle a logarithmic layer emerges first for $\beta = 0.60$ at about $t = 3\pi/2$ and later even for $\beta = 0.75$ and $\beta = 0.85$. Therefore, in the negative half-cycle the situation is reversed with respect to the positive one. Once again the logarithmic layer persists during most of the decelerating phase. Figure 7 shows that the equation $\langle u\rangle^+ = \log(y^+)/k + A$, with $k = 0.41$ and $A = 5$, is in a fairly good agreement with present results where a logarithmic layer is detected. For a sinusoidally oscillating flow Jensen *et al.* (1989) reported that the constants of the log-law at $R_\delta = 3464$ are

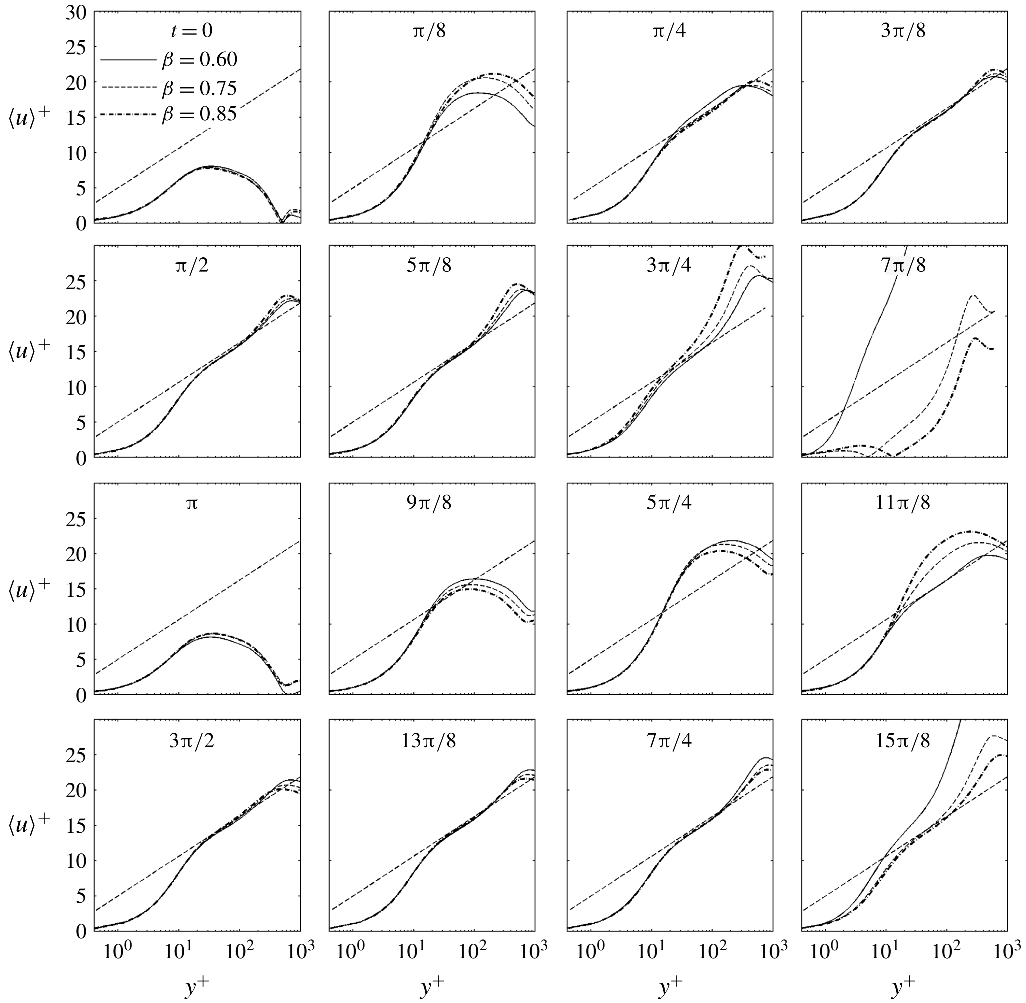

FIGURE 8. Ensemble-averaged velocity profiles in semi-log plot during the period for $R_\delta = 1414$. Thin dashed line: $\langle u \rangle^+ = \log(y^+)/0.41 + 5$.

$k = 0.4$ and $A = 5$, while Salon *et al.* (2007) for $R_\delta = 1790$ reported $k = 0.41$ and A phase dependent, with $A = 5$ for $2\pi/3 < t < 5\pi/6$. Therefore, present results are consistent with those found by previous investigations on unsteady flows. Figure 8 shows the semi-log plot of the velocity profiles for $R_\delta = 1414$. It can be noted that an increase of R_δ shifts back the phase of occurrence of a logarithmic layer. Compare for example figures 7 and 8 at $t = \pi/4$.

3.2. *Turbulent structures*

Flow visualizations of the near-wall region of a steady turbulent boundary layer (Kline *et al.* 1967; Corino & Brodkey 1969) have shown that it is characterized by low- and high-speed streaks of fluid, mostly aligned with the streamwise direction and having a mean spacing of approximately $100\nu^*/u^*_\tau$, where u^*_τ is the friction velocity. These turbulent structures are now recognized to be ubiquitous features of wall turbulent flows and essential in the process of generation and sustenance of turbulence (Schoppa & Hussain 2002). Low-speed streaks have also been observed in sinusoidally oscillating boundary layers by Fishler & Brodkey (1991), Costamagna *et al.* (2003) and Salon *et al.* (2007). As shown in the following, the time development of the wall shear stress is strongly affected by the dynamics of the streaks, thus any insight on these turbulent structures contributes to a better understanding of the spatial and temporal distribution of the turbulent skin friction.

In figure 9 the fluctuation u' of the streamwise velocity component, computed by subtracting to the local velocity u the streamwise velocity averaged in the (x, z) plane, is shown at four phases during the first half-cycle, in the plane placed at $y=0.16$, for $R_\delta = 1100$ and $\beta = 0.60$, 0.75 and 0.85. In terms of wall units, the position of the plane corresponds to $y^+ \approx 10$ at the phase of the peak of τ_0. Figure 9 shows that no streaks can be detected at the beginning of the cycle. Focusing attention on $\beta = 0.60$ (*a*–*d*), the streaks emerge between $t=0$ and $t=\pi/8$ and in the interval $\pi/8 - \pi/4$ they attain a well-developed state, spanning the entire fluid domain. Between $t=\pi/4$ and $t=3\pi/8$ the streaks begin to meander and interact among themselves until they break down and split into short segments, which mostly remain aligned with the streamwise direction. The onset of breaking occurs during the accelerating phase, i.e. before the peak of the free stream velocity. The breaking propagates in space causing a rapid increase of the plane-averaged wall shear stress. When β increases both the phase of appearance and breaking of the streaks are shifted back. The panel in figure 9, for $\beta = 0.75$ and $t=\pi/4$, shows that breaking down of streaks is in progress in the fluid domain, since it is occurring in certain areas of the domain while outside these areas the streaks still show an elongated shape. The low-speed streaks disappear near the flow reversal and reappear during the accelerating phase of the negative half-cycle (not shown). Both the reappearance and the breakdown occur earlier for lower values of β, therefore, in this regard, in the negative half-cycle the situation is reversed with respect to the positive one.

There is a general consensus in the scientific community that the streaks are generated by a sequence of streamwise vortices, which follow each other and pump low-speed fluid away from the wall and high-speed fluid towards the wall. While these vortices are advected downstream, they leave behind a streak of low-speed fluid (Robinson 1991; Hamilton, Kim & Waleffe 1995; Moin & Mahesh 1998; Schoppa & Hussain 2002). Within this framework, theories have been developed to describe the regeneration mechanism of turbulence according to which the low-speed streaks instability generates new vortical structures which in turn sustain the streaks (Schoppa & Hussain 2002).

In order to gain insights about the process that leads to the streak appearance and breakdown in the flow under investigation, the low-speed regions along with the vortex structures are shown in a three-dimensional plot in figure 10 at six phases during the first half-cycle for $R_\delta = 1100$ and $\beta = 0.75$. The vortex cores are identified by means of the method of Jeong & Hussain (1995), according to which they are localized in the regions characterized by two negative eigenvalues of the symmetric tensor $\boldsymbol{D}^2 + \boldsymbol{\Omega}^2$, where $\boldsymbol{D}$ and $\boldsymbol{\Omega}$ denote the symmetric and antisymmetric parts of the velocity gradient tensor respectively. Therefore, negative values of the second eigenvalue λ_2 $(\lambda_1 > \lambda_2 > \lambda_3)$ identify the vortex cores.

Figure 10(*a*) shows the turbulent structures a short time after the free stream velocity reverses its direction. Several vortices, remnant of the previous half-cycle and devoid of any type of organization, can be observed along with blobs of fluid characterized by low streamwise velocity. Because of the shear of the mean flow,

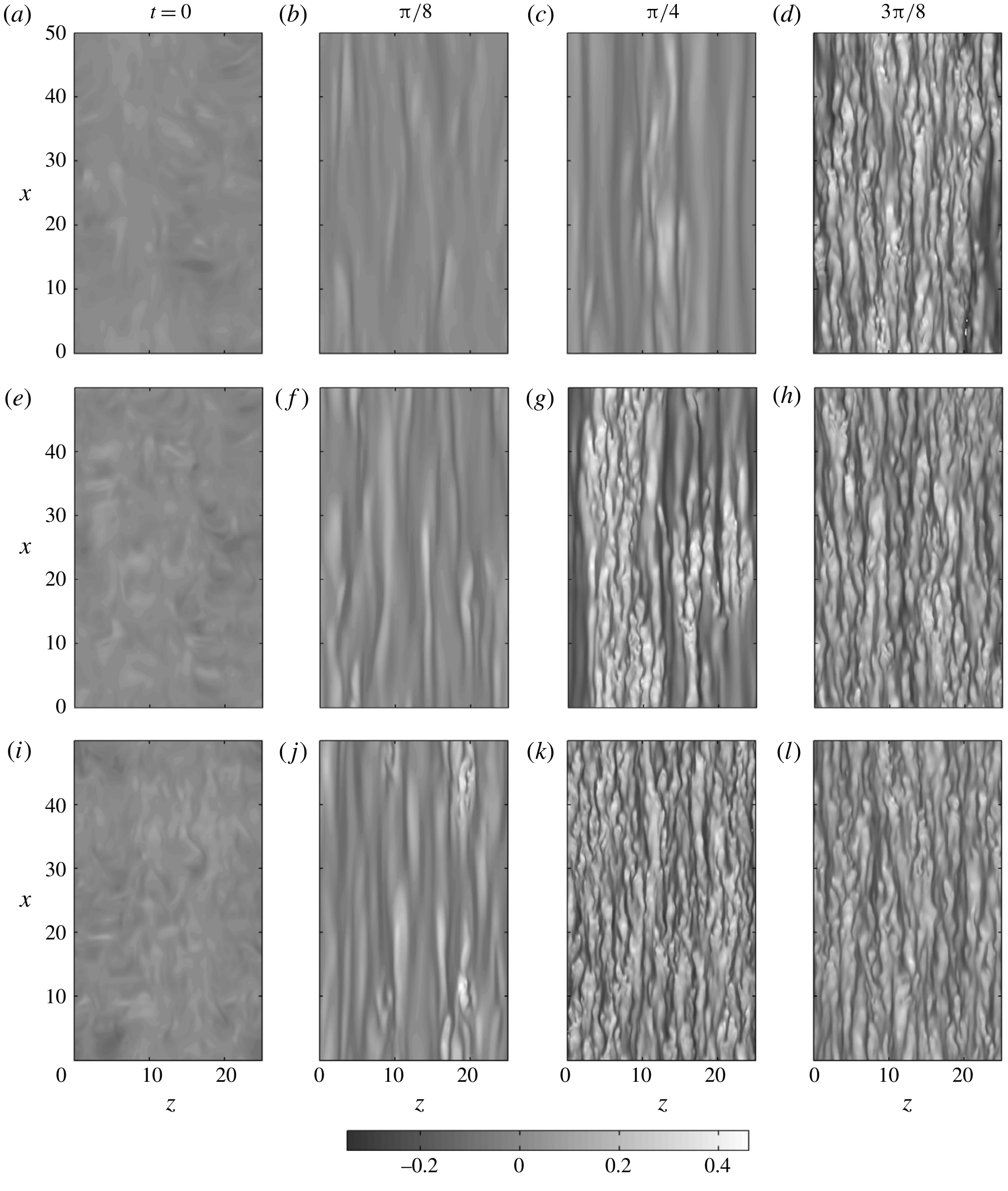

FIGURE 9. Low-speed streaks for $R_\delta = 1100$ in the plane $y = 0.16$. Darker areas denote the low-speed streaks. (*a–d*) $\beta = 0.60$; (*e–h*) $\beta = 0.75$; (*i–l*) $\beta = 0.85$.

several vortex structures are tilted towards the x direction and stretched, causing an increase of the streamwise vorticity component. These vortices affect the wall-normal distribution of streamwise momentum through the ejection of slow fluid away from the wall, according to the previously described mechanism. Thus for example a newly formed streak with the tip at about $(x, z) \approx (10, 15.3)$ can be observed in figure 10(*a*). As the flow evolves, the streaks and the streamwise vortices grow and strengthen as shown in figure 10(*b*), where the previously mentioned streak has the tip at approximately $(x, z) \approx (30, 15.3)$. The growth occurs through a mechanism that

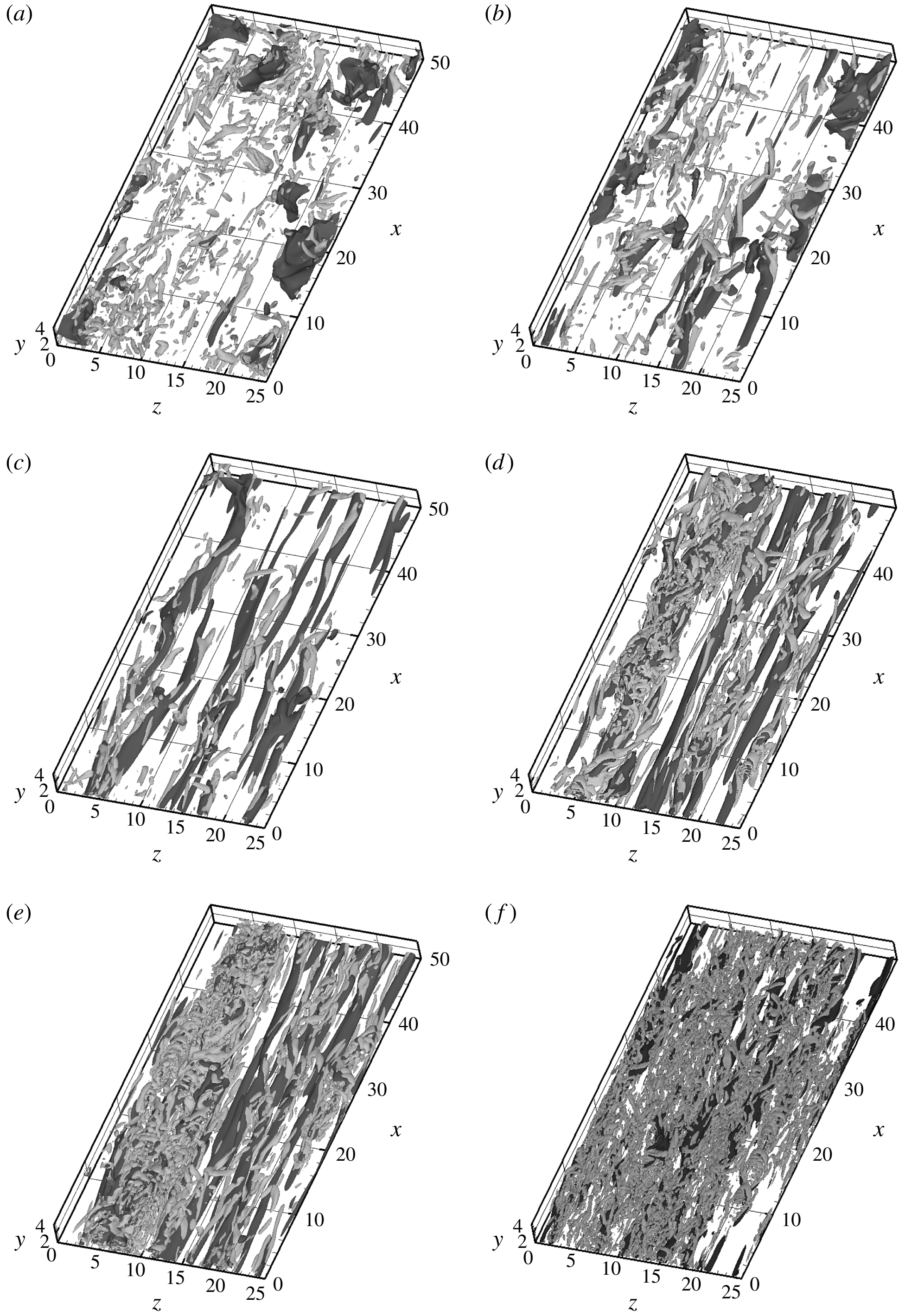

FIGURE 10. Evolution of the low-speed streaks and of the vortex structures during the first half-cycle for $R_\delta = 1100$ and $\beta = 0.75$. Darker regions denote the low-speed streaks; grey regions are the isosurfaces of second eigenvalue λ_2 and denote the vortex cores; (*a–e*): $\lambda_2 = -0.007$, $u' = -0.08$; (*f*) $\lambda_2 = -0.04$, $u' = -0.16$; (*a*) $3\pi/64$, (*b*) $5\pi/64$, (*c*) $\pi/8$ (*d*) $3\pi/16$, (*e*) $13\pi/64$, (*f*) $\pi/4$.

feeds both the vortices and the streaks. Because of the y gradient of the u velocity component, the wall-normal vorticity induced by the presence of the streaks is tilted in the x direction, thus it feeds the streamwise vortex structure. However, as shown by the analysis of Schoppa & Hussain (2002), the main contribution to the production of streamwise vortices comes from the stretching of sheets of streamwise vorticity because of $\partial u/\partial x$ velocity gradient induced by the streak waviness in (x, z) planes. These authors also identified a 'streak transient growth mechanism' able to amplify x-dependent disturbances and thus able to produce large streamwise velocity gradients. Once the streamwise vortices have grown substantially, in turn they sustain the streaks through the ejection mechanism. This explains why in figure 10(*c*) the streaks are surrounded by vortices. These turbulent structures gradually develop during the accelerating phase up to $t \approx 3\pi/16$ when an explosive growth of both streaks and vortices accompanied by a random motion occurs (see figure 10*d*). More specifically, the low-speed streaks in the left part of figure 10(*d*) $(0 < z < 12)$ undergo a wavy motion followed by the development of several vortices, some of them being quasi-longitudinal in shape while others have the shape of arches that wrap around the low-speed streaks. The ensemble of all these turbulent structures is called a turbulent spot and has been studied experimentally by Carstensen *et al.* (2010) for the case of a Stokes layer. According to these experiments, the turbulent spots are areas characterized by large turbulent fluctuations, separated by the rest of the space by sharp fronts. The authors found that the spots first emerge in the form of two longitudinal streaks which then break into small turbulent structures. Figure 10(*c*,*d*) show that a similar phenomenon occurs in this flow as the turbulent spot appears in $0 < z < 12$ where two low-speed streaks are initially present in figure 10(*c*). Breaking of the low-speed streaks is then associated with the emergence of turbulent spots. Here, this can be better demonstrated by a comparison between figures 9 and 10. In figure 10(*c*) no turbulent spots are detected, hence in figure 9(*f*), at $t = \pi/8$, the streaks are still intact. The turbulent spot that for the first time appears in figure 10(*d*), affects almost the entire fluid domain in figure 10(*f*). In figure 9(*g*), at the same instant of figure 10(*f*) $(t = \pi/4)$, the streaks are broken down over a large part of the domain.

In addition to the turbulent spots, Carstensen *et al.* (2010) detected two-dimensional vortex structures, denoted as vortex tubes, produced as a result of the flow instability due to an inflection point in the laminar velocity profile (Carstensen *et al.* 2010; Scandura 2013). An inflection point is also apparent in the mean velocity profiles of the turbulent flow shown in figure 5, however, vortex tubes have not been observed here. The reason for this result is most likely due to the fact that in turbulent flow, the wall-normal gradient of $\langle u \rangle$ at the inflection point is much smaller than in laminar flow, therefore, the instability is not triggered.

Figure 11 shows the fluctuating velocity components (u', v', w') along the spanwise direction, at $x = 12.5$ and $y = 0.16$, for $\beta = 0.75$, $R_\delta = 1100$ and $t = \pi/8$, when low-speed streaks are present in the flow. Figure 11(*a*) is cropped from figure 9, for $\beta = 0.75$ and $t = \pi/8$, and shows the streaks in the range $12 < x < 13$. The vertical velocity component is very low at $y = 0.16$, therefore in figure 11 it has been magnified by 10 times in order to make it comparable with the others. The trend of u' shows nine low-speed streaks which mostly occur in concomitance with positive values of v'. This shows that the low-speed streaks are generated by an upward motion of slow fluid, in agreement with the previously described mechanism that involves streamwise vortices. Unlike the wall-normal component, w' does not appear to be well correlated with u'. However, it can be observed that close to each position

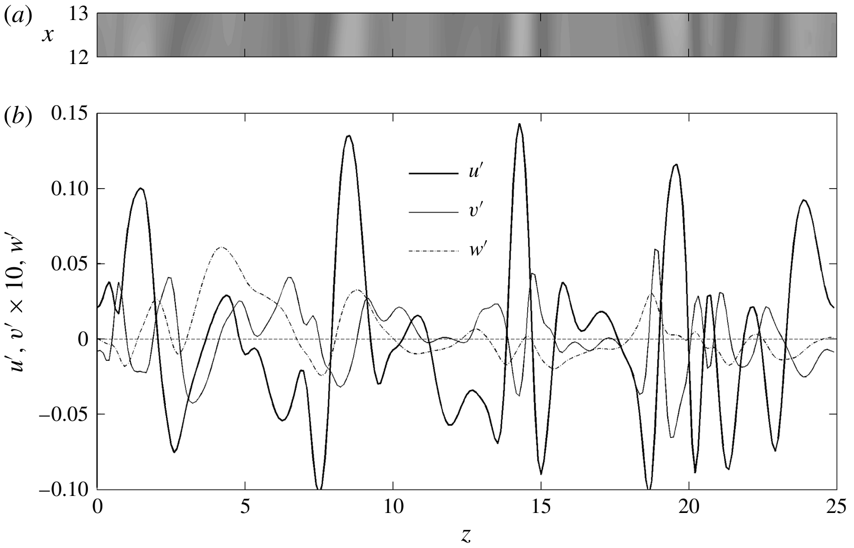

FIGURE 11. (*a*) Low- and high-speed streaks in the range $12 < x < 13$; darker areas denote low-speed streaks: see figure 9 for the contour map legend. (*b*) Trend of the velocity fluctuations along the spanwise direction at $x = 12.5$ and $y = 0.16$. $R_\delta = 1100$, $\beta = 0.75$, $t = \pi/8$.

where the vertical velocity vanishes, the spanwise velocity has a local maximum or a local minimum. This is a feature of the flow field generated by a streamwise vortex, as can be easily checked.

Studies concerning steady turbulent boundary layers and channel flows have shown that the spacing Δ^+ between low-speed streaks ranges from 80 to 120 wall units (Pope 2000). For a sinusoidally oscillating flow Costamagna *et al.* (2003) reported $\Delta^+ = 127$ at $R_\delta = 800$ while Salon *et al.* (2007) reported $\Delta^+ = 110$ at $R_\delta = 1790$. Of course, because of the flow unsteadiness, the spacing between low-speed streaks varies during the cycle. In this study Δ^+ has been determined by computing the spanwise autocorrelation function of the fluctuating streamwise velocity component u'. An estimate of the low-speed streak spacing is given by two times the separation at which the correlation attains the minimum. In figure 12 the streaks spacing expressed in wall units ($\Delta^+ = \Delta\sqrt{\tau_0}R_\delta$), computed by phase averaging over all the available cycles, is shown when low-speed streaks are detected, even though they are broken into short segments, not spanning the entire fluid domain. As shown in figure 9, no low-speed streaks are observed in a neighbourhood of the flow reversal, therefore in figure 12 no data are reported at $t = 0$ and $t = \pi$. Figure 12(*a*) shows that at $t = \pi/8$ the spacing increases both for $\beta = 0.60$ and $\beta = 0.75$. Such an increase is due to the merging of neighbouring streaks. An analogous increase of Δ^+ is not observed for $\beta = 0.85$ because of the large acceleration that characterizes this case, which anticipates the break up of the streaks. After breaking, the spacing takes values within $100 - 110$ up to $t \approx 3\pi/4$. For $R_\delta = 1414$ (figure 12*b*) no increase of the streak spacing is observed at the beginning of the positive half-cycle as a larger Reynolds number shifts back the onset of breaking. Even for $R_\delta = 1414$ the spacing is within 100–110 just after the streaks break. The spacing however increases towards the end of the decelerating phase because of the coalescence of neighbouring streaks,

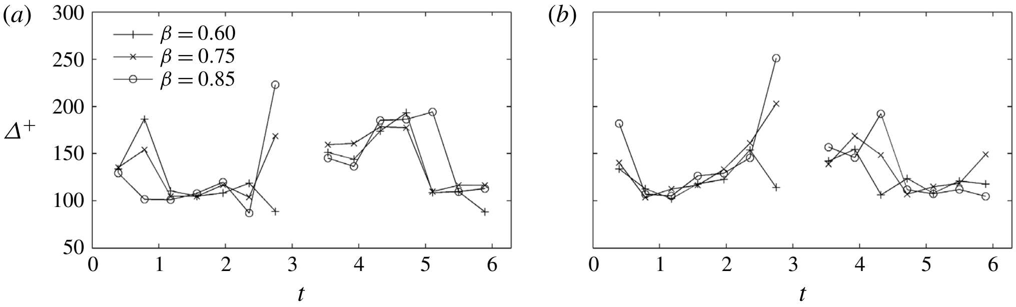

FIGURE 12. Mean spacing between two low-speed streaks during the period. (*a*) $R_\delta = 1100$; (*b*) $R_\delta = 1414$.

thus assuming a value of approximately 125 at $t = 3\pi/4$. This phenomenon is more important for conditions characterized by a slower deceleration such as $\beta = 0.75, 0.85$.

In the negative half-cycle the streaks can be already observed at $t = 9\pi/8$ with a large spacing in between that persists for a longer time in comparison to the positive half-cycle. This result is due to the low acceleration of the negative half-cycle which leaves more time to the streaks before reaching the instability condition which causes them to break. After breaking has occurred the spacing decreases up to a value of approximately 110. In summary, when the streaks are broken into short segments the spacing is in the range of 100–110 wall units, while in the other phases the spacing ranges between 100–200 wall units.

3.3. *Turbulent kinetic energy and Reynolds stress*

The contour plot of the turbulent kinetic energy $k = (\langle u'^2\rangle + \langle v'^2\rangle + \langle w'^2\rangle)/2$ in the (t, y) plane is shown in figure 13. It can be noted that during the accelerating phase of the positive half-cycle the turbulent kinetic energy becomes large near the wall first and then away from it. This is a consequence of the closeness to the wall of the peak of production of turbulent kinetic energy, as illustrated in figure 14. Indeed, large values of k appear away from the wall only after convection and diffusion have acted for a sufficiently long time. The intense production of k that occurs during the accelerating phase, generates both large time derivatives and large y gradients near the wall. During the decelerating phase, because of the decrease of production, both the time derivative and the y gradient become relatively small.

The peaks of the turbulent kinetic energy fall in the range $y = 0.2$–0.3, and precede the peaks of the free stream velocity, both during the positive and the negative half-cycle. In the positive half-cycle the larger is β the sooner the maximum of k occurs, while the opposite is observed in the second half-cycle. An increase of β brings the maximum of the negative half-cycle closer to that of the next positive half-cycle. For $R_\delta = 1100$ the peaks of the turbulent kinetic energy range from 0.0134 to 0.0157, while for $R_\delta = 1414$ they range from 0.0094 to 0.0139. The ratio of the first peak to the second one increases both with acceleration skewness and Reynolds number and ranges from 1.04 to 1.48. Even though the maximum of k occurs in the positive half-cycle, during the negative half-cycle the turbulent kinetic energy spreads at larger distances from the wall than in the positive half-cycle. This result is explained by the longer duration of the acceleration phase of the negative half-cycle, which leaves more time for the turbulent kinetic energy to spread away from the wall.

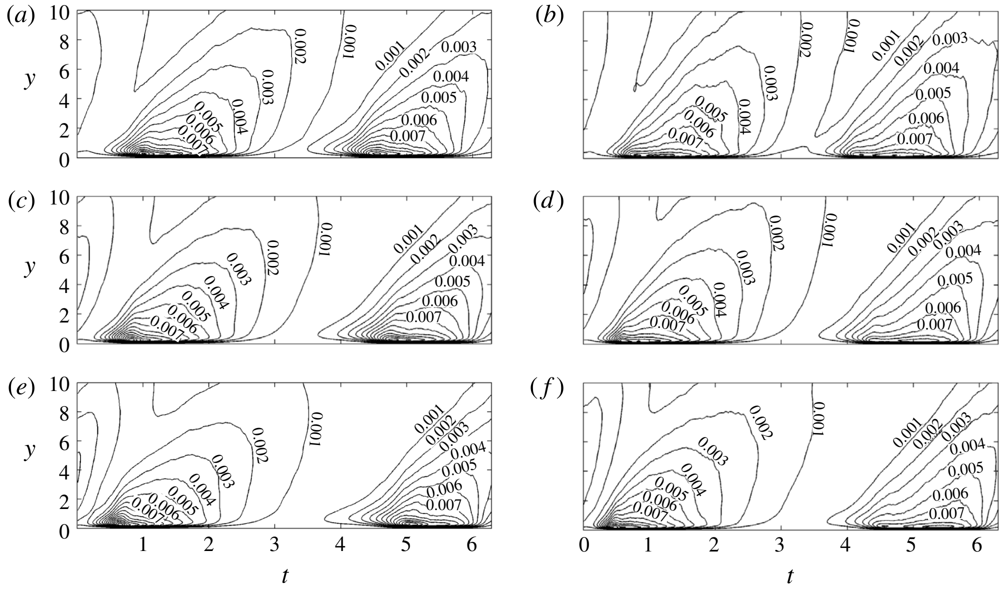

FIGURE 13. Turbulent kinetic energy k as a function of the time t and of the y coordinate. Contour interval: 10^{-3}. (a,c,e) $R_\delta = 1100$; (b,d,f) $R_\delta = 1414$; (a,b) $\beta = 0.60$; (c,d) $\beta = 0.75$; (e,f) $\beta = 0.85$.

A quantitative assessment of the mechanisms affecting the turbulent kinetic energy can be provided by means of the turbulent kinetic energy budget, which in dimensionless form reads:

$$\begin{aligned}\frac{\partial k}{\partial t} &= -\frac{R_\delta}{2}\langle u_1' u_2'\rangle \frac{\partial \langle u_1\rangle}{\partial x_2} - \frac{R_\delta}{2}\frac{\partial}{\partial x_2}\left(\frac{1}{2}\langle u_j' u_j' u_2'\rangle\right) - \frac{R_\delta}{2}\frac{\partial \langle p' u_2'\rangle}{\partial x_2} \\ &\quad + \frac{\partial}{\partial x_2}\langle u_j' s_{j,2}\rangle - \langle s_{j,\ell} s_{j,\ell}\rangle, \end{aligned} \tag{3.3}$$

where $s_{j,\ell} = (\partial u_j'/\partial x_\ell + \partial u_\ell'/\partial x_j)/2$. The terms contributing to the right-hand side of (3.3) from left to right are: production of turbulent kinetic energy, turbulent convection, pressure transport, viscous diffusion and dissipation ϵ. In figure 14, where such terms are shown at 16 phases during the cycle for $R_\delta = 1100$ and $\beta = 0.75$, it can be observed that all these contributions are important in a thin layer near the wall, approximately $1.5\delta^*$ thick. The pressure transport term is always much smaller than the other terms, while viscous diffusion and turbulent convection are both important and of the same order of magnitude, except near the wall, where the turbulent convection vanishes. In order to provide a comprehensive picture of the time variation during the period of production and dissipation of the turbulent kinetic energy, (3.3) have been integrated between $y = 0$ and $y = L_y$ and the results have been reported in figure 15(a,b) as a function of time. Here I_p and I_ϵ denote the integral of turbulence production and dissipation respectively, which are the only two terms, belonging to the right-hand side of (3.3), that do not vanish after integration. Figure 15(a) shows that turbulence production and dissipation rapidly increase at the beginning of the cycle, first for large β. During the decelerating phase I_p and I_ϵ decay and both take low values in the central part of the period. In the negative

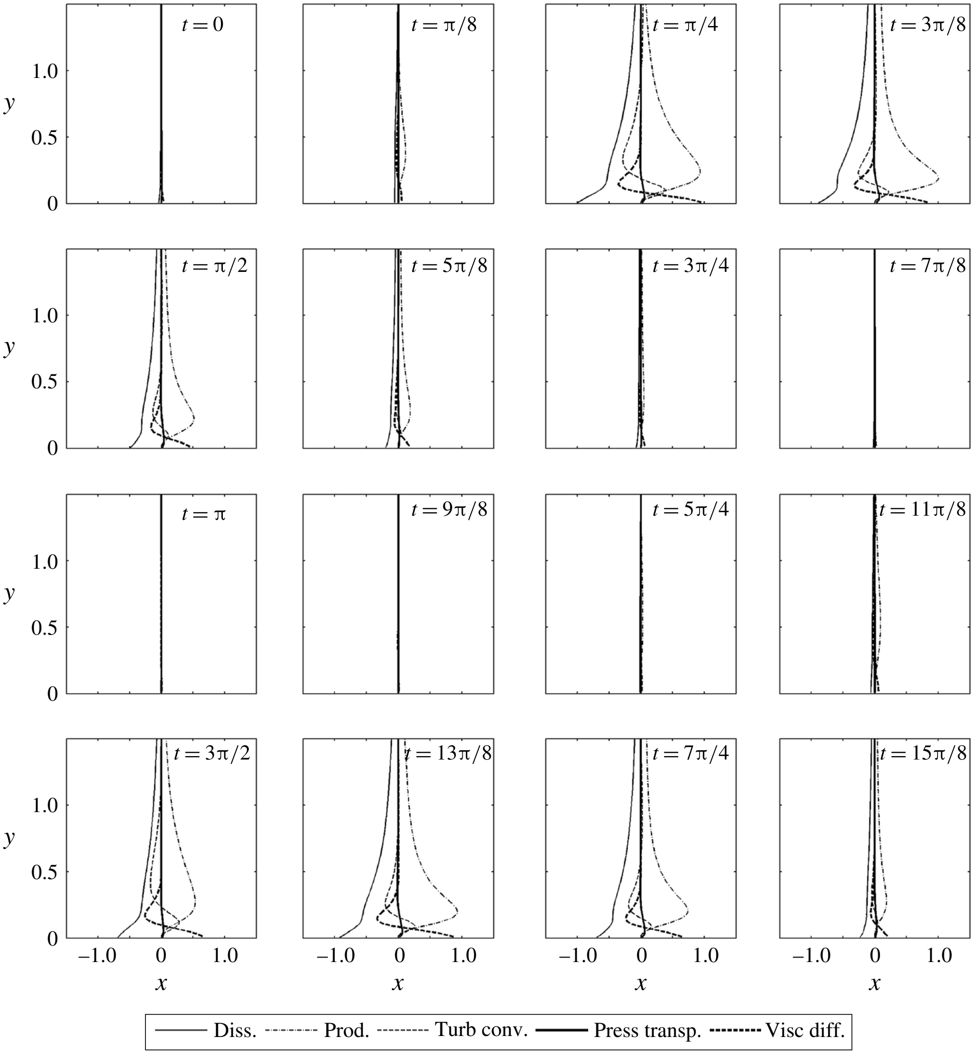

FIGURE 14. Terms of the turbulent kinetic energy budget at 16 phases during the wave cycle for $\beta = 0.75$ and $R_\delta = 1100$.

half-cycle they increase again but, in contrast to the positive one, such an increase is more rapid for lower values of β. The increase of the Reynolds number expands the fraction of the cycle in which production and dissipation are both important, as it can be observed by comparing figure 15(*a*) with figure 15(*b*).

In figure 15(*c*,*d*) the quantity $I_\epsilon + I_p$ is shown along with the trend of the time derivative of the turbulent kinetic energy integrated along the y direction $\partial I_k/\partial t$. Because of the form of (3.3) and of the boundary conditions, $\partial I_k/\partial t$ must be equal to $I_\epsilon + I_p$. Indeed, figure 15(*c*,*d*) shows that these quantities are in a fairly good agreement. The small discrepancies arise from unavoidable artificial dissipative effects due to the numerical scheme adopted for the time advancement of the governing equations. Figure 15(*c*) shows that during the accelerating phase of the positive half-cycle $\partial I_k/\partial t$ increases rapidly, attains a maximum and then decreases up to

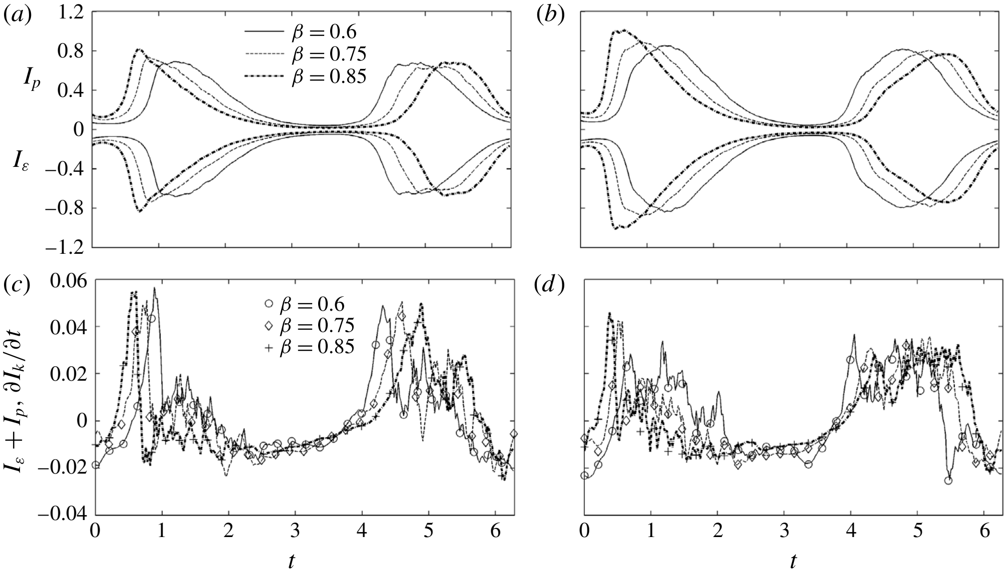

FIGURE 15. (*a*,*c*) $R_\delta = 1100$, (*b*,*d*) $R_\delta = 1414$. (*a*,*b*) Production and dissipation of turbulent kinetic energy integrated along the y direction. Here I_p and I_ϵ denote the integral of production and dissipation respectively. (*c*,*d*) The lines denote $I_p + I_\epsilon$ while the markers denote the time derivative of the turbulent kinetic energy integrated along the y direction $\partial I_k/\partial t$.

a minimum. The rapid increase begins when the low-speed streaks still have an elongated shape (see figure 9), while the maximum occurs near the onset of streaks breaking. Prior to this event, the flow quantities, such as the wall shear stress, are scarcely affected by the turbulence. After the streaks begin to break, small-scale vortices characterized by a large dissipation of turbulent kinetic energy are generated, therefore the time derivative of the spatially integrated turbulent kinetic energy rapidly decreases.

In the negative half-cycle the trend of $\partial I_k/\partial t$ shows differences with respect to the first half-cycle due to the acceleration skewness. For example, the first peak is smaller than that in the positive half-cycle, but later larger values than those of the positive half-cycle occur. Figure 15(*d*) shows that for $R_\delta = 1414$ the value of $\partial I_k/\partial t$ related to the first maximum and those at later phases in the same half-cycle are closer to each other than those at $R_\delta = 1100$. The anticipation of streaks breaking during the cycle due to the larger Reynolds number explains such a result as $\partial I_k/\partial t$ has a shorter time to grow.

Insights about the distribution of the turbulent kinetic energy among the different spatial scales and for the three velocity components are given in figure 16 where the one-dimensional longitudinal and transverse energy spectra along the x direction at $y = 1$ are shown for $R_\delta = 1414$ and $\beta = 0.75$. The equations of the Kolmogorov spectra that characterize the inertial sub-range of a statistically stationary homogeneous isotropic turbulence (Pope 2000) are also shown in figure 16. Such equations have the following dimensionless form:

$$E_{11} = c\left(\frac{R_\delta}{2}\right)^{-2/3}\epsilon^{2/3}k_x^{-5/3}, \quad E_{22} = E_{33} = c_1\left(\frac{R_\delta}{2}\right)^{-2/3}\epsilon^{2/3}k_x^{-5/3}, \qquad (3.4a,b)$$

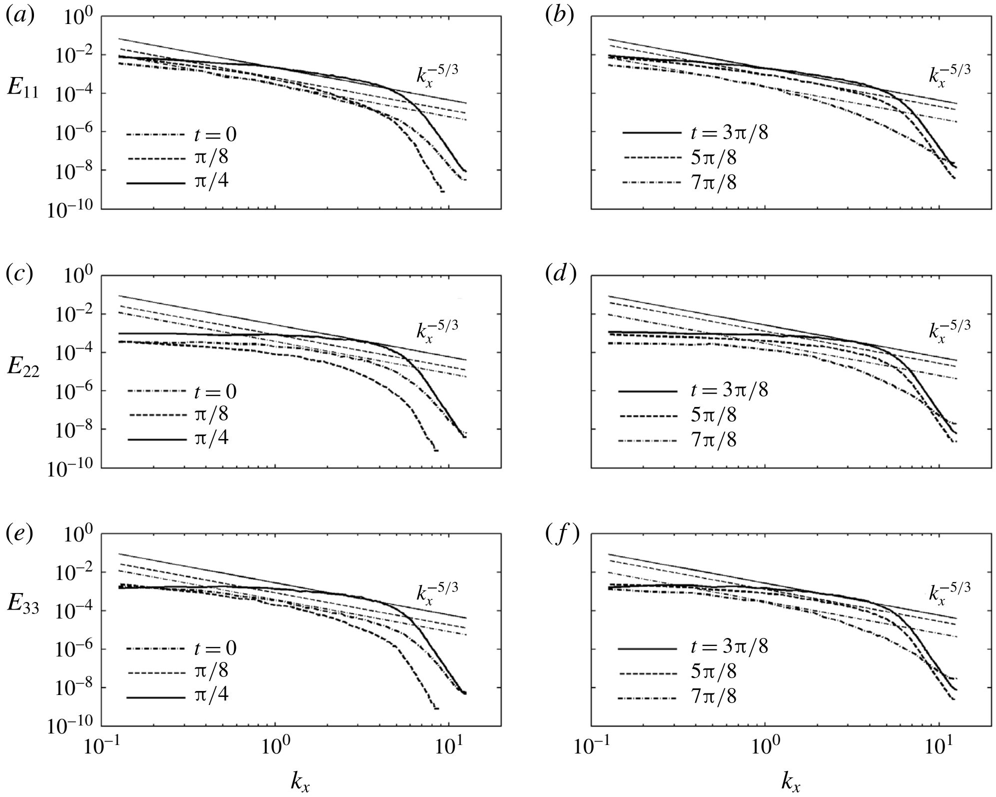

FIGURE 16. Energy spectra along the streamwise direction at six phases during the positive half-cycle for $R_\delta = 1414$ and $\beta = 0.75$. The straight lines are described by (3.4).

where $c \approx 0.49$ and $c_1 \approx 0.65$. The dissipation ϵ is evaluated at the specified y position. Figure 16 shows that the spectra match the Kolmogorov spectra within a short range of wavenumbers. The shortness of such a range is justified by the relatively low Reynolds number. For E_{11} the agreement with (3.4) is fairly good for all the phases shown in figure 16, while for E_{22} and E_{33} an agreement occurs at the phases of well-developed turbulence ($\pi/4$, $3\pi/8$), but even at $t = 0$ for E_{22} and during the deceleration for E_{33}. It is interesting to note that according to (3.4), where an inertial sub-range is present, the spectra E_{22} and E_{33} are equal to each other, therefore significant differences between them may arise only for wavenumber that are quite far away from the inertial sub-range. Figure 16 also shows that at low wavenumbers the longitudinal spectrum E_{11} is larger than the E_{22} and E_{33} spectra. For large k_x E_{11} is still the largest, apart from $t = 0$ and $t = 7\pi/8$ where E_{33} is slightly larger than E_{11}. A comparison between E_{33} and E_{22} shows that for small k_x the former is larger than the latter, while at large wavenumbers they are close to each other. Therefore, it emerges that E_{22} takes smaller values than the other spectra, especially close to the phases of flow reversal. The spectra do not change significantly in the interval $\pi/4 - 3\pi/8$, thus suggesting that despite the flow unsteadiness, the contribution to the turbulent intensity from the different spatial scales is rather constant in time during this range of phases.

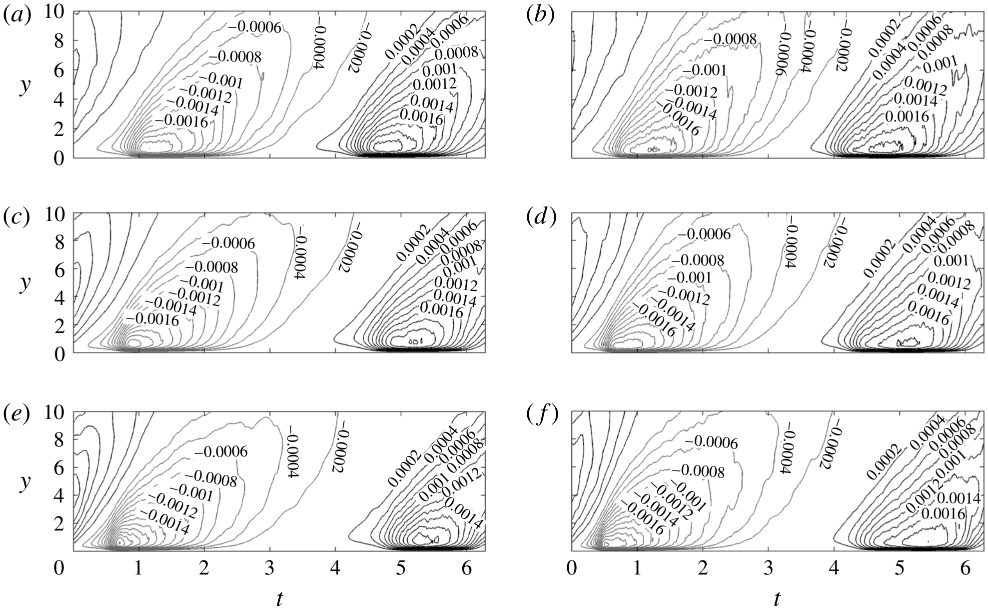

FIGURE 17. Reynolds stress $\langle u'v' \rangle$ as a function of the time t and of the y coordinate. Black lines: positive values, grey lines: negative values. Contour interval: 2×10^{-4}. (*a*,*c*,*e*) $R_\delta = 1100$; (*b*,*d*,*f*) $R_\delta = 1414$; (*a*,*b*) $\beta = 0.60$; (*c*,*d*) $\beta = 0.75$; (*e*,*f*) $\beta = 0.85$.

In figure 17 the space–time contour plot of the Reynolds stress $\langle u'v' \rangle$ during the flow cycle is shown. Here comments similar to those already made for the turbulent kinetic energy could be repeated. The peaks of the Reynolds stress fall in the range $y = 0.44$–0.70 and precede those of the free stream velocity both during the positive and the negative half-cycle. The negative peaks range from -0.0028 to -0.0024 while the positive ones range from 0.0022 to 0.0024. In the negative half-cycle large absolute values of the Reynolds stress are found at distances further away from the wall compared to those in the positive half-cycle, similarly to the turbulent kinetic energy shown in figure 13.

One of the important consequences of acceleration skewness is that the period average of the Reynolds stress $\overline{\langle u'v' \rangle}$ does not vanish. In figure 18(*a*–*c*), where the period-averaged Reynolds stress profiles are shown, it can be observed that the magnitude of $\overline{\langle u'v' \rangle}$ is large near the wall and rapidly decreases as y increases. In the presence of a non-vanishing $\overline{\langle u'v' \rangle}$, the balance of the period-averaged momentum is satisfied thanks to the viscous stress generated by a steady streaming in the boundary layer (Scandura 2007). The trend of the steady streaming is shown in figure 18(*d*–*f*). It can be observed that for the smallest value of acceleration skewness the difference between the two Reynolds numbers is not significant, while it becomes more apparent when the acceleration skewness is larger. Interestingly, for large β an increase of the Reynolds number causes a decrease both of the period-averaged Reynolds stress and of the steady streaming. On the basis of this result one might infer that for very large Reynolds numbers the steady streaming vanishes, as in a laminar flow. However, to draw plausible conclusions in this regard, data at much larger Reynolds number than those here considered are necessary.

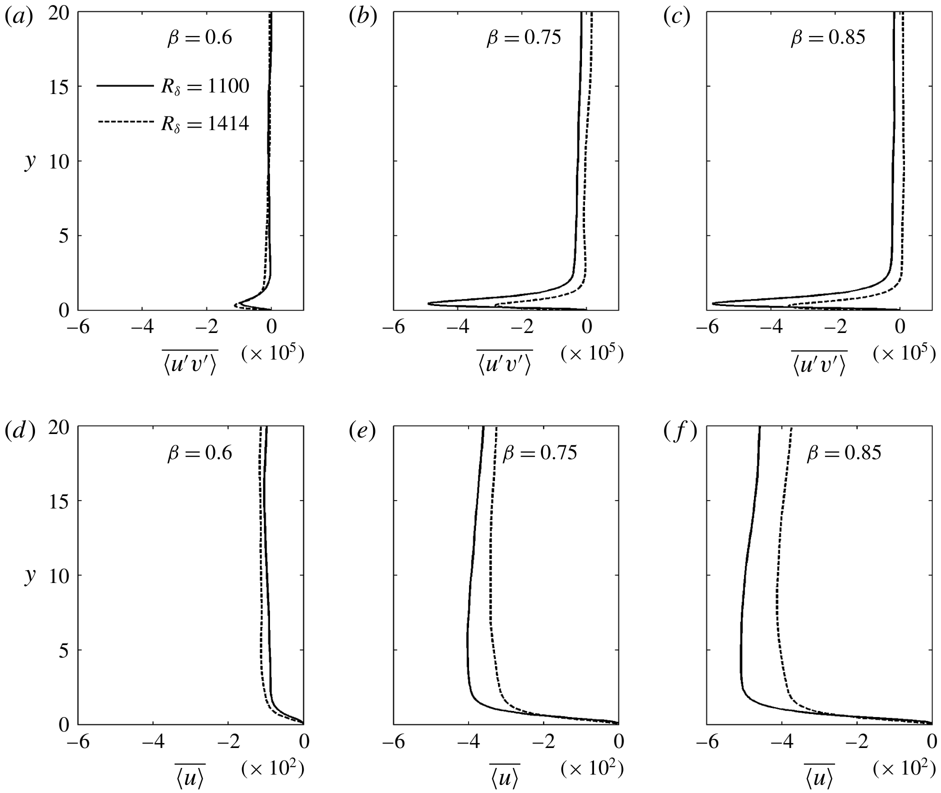

FIGURE 18. (*a–c*) Period average of the Reynolds stress $\overline{\langle u'v' \rangle}$; (*d–f*) period average of the ensemble-averaged streamwise velocity $\overline{\langle u \rangle}$.

3.4. *Wall shear stress statistics*

In § 3.1 the wall shear stress has been analysed mainly focusing on its ensemble average. Here the analysis is extended with the aim of gaining insights about its spatial distribution and statistics. In figure 19 the spatial distribution of the streamwise and spanwise components of the wall shear stress fluctuations for $R_\delta = 1100$ and $\beta = 0.75$ are shown at four phases during the positive half-cycle. The fluctuations along the streamwise direction τ_x' are computed by subtracting from the wall shear stress τ_x its spatial average, while the fluctuations in the spanwise direction are equal to the wall shear stress τ_z, since the spatial average vanishes. Figure 19(*a*,*b*) show small areas characterized by large fluctuations, outside of which the wall shear stress takes values close to those in laminar flow. A comparison between figure 10(*d–f*) $(0 < z < 12)$ and figure 19(*a–c*) respectively, shows that within a turbulent spot the wall shear stress fluctuations are large. Moreover, comparing figure 19(*c*,*g*) with figure 9 for $\beta = 0.75$ and $t = \pi/4$, it can be observed that large fluctuations of the wall shear stress are detected where breaking of the low-speed streaks has occurred. Therefore, the areas characterized by large fluctuations shown in figure 19 are the imprint of the turbulent spot and they also correspond to the areas where the low-speed streaks are broken into short segments.

A comparison between figure 3(*a*) for $\beta = 0.75$ and figure 10 shows that the rapid increase of the ensemble-averaged wall shear stress begins with the appearance

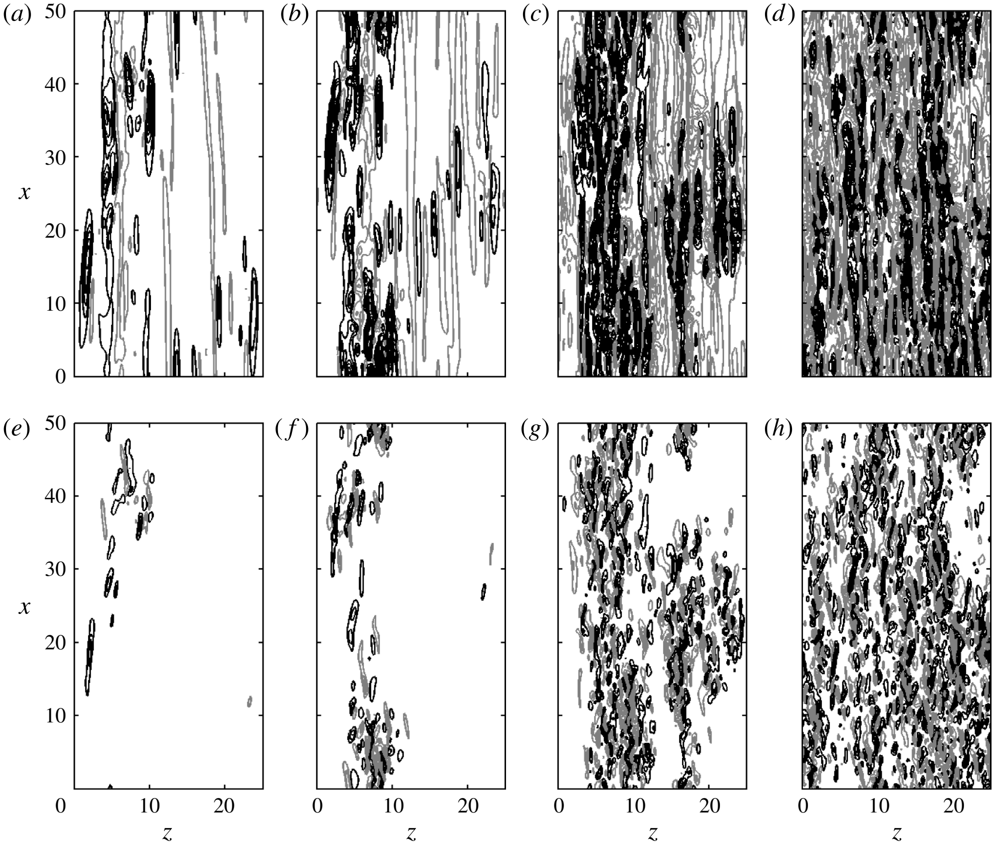

FIGURE 19. Wall shear stress fluctuations for $R_\delta = 1100$ and $\beta = 0.75$. (*a*,*e*) $t = 3\pi/16$; (*b*,*f*) $t = 13\pi/64$; (*c*,*g*) $t = \pi/4$; (*d*,*h*) $t = 9\pi/32$. Streamwise wall shear stress fluctuations τ_x': (*a*) (min, max) = (−0.0012, 0.0042); (*b*) (−0.0015, 0.0097); (*c*) (−0.0027, 0.0156); (*d*) (−0.0033, 0.0125). Spanwise wall shear stress τ_z: (*e*) (min, max) = (−0.002, 0.0019); (*f*) (−0.0045, 0.0068); (*g*) (−0.0058, 0.0041); (*h*) (−0.0074, 0.0074). Black lines: positive values; grey lines: negative values. Contour interval: 5×10^{-4}. The fluid oscillates along the x direction.

of the turbulent spots ($t \approx 3\pi/16$) and ends when they spread in the whole fluid domain, which occurs at approximately $t = 9\pi/32$. Since within the turbulent spots the fluctuations of the wall shear stress are large, in the presence of a wall made up by loose material, the mobilization of clusters of sediments has a high probability to occur. However, defining the condition of incipient motion of such sediments would be particularly difficult because the turbulent spots are randomly distributed in the space and they do not appear exactly at the same phase in every cycle. Concerning the spatial distribution of the spanwise wall shear stress, from figure 19 it seems to emerge that τ_z takes significant values mainly where τ_x' is positive. This issue will be addressed in the following by means of a more objective approach.

The statistical parameters here considered to characterize the wall shear stress are: the relative intensity $R_x = \sigma_{\tau_x}/\tau_0$, where $\sigma_{\tau_x} = \langle \tau_x'^2 \rangle^{1/2}$ is the r.m.s. of the wall shear stress fluctuations, the skewness coefficient $S_x = \langle \tau_x'^3 \rangle / \sigma_{\tau_x}^3$ and the flatness coefficient

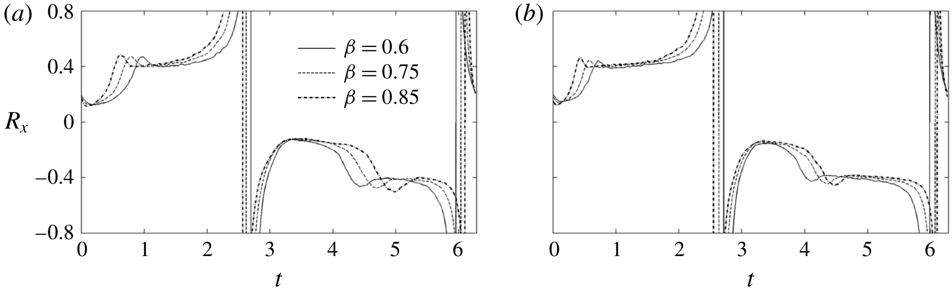

FIGURE 20. Relative intensity $R_x = \sigma_{\tau_x}/\tau_0$ of the wall shear stress along the x direction during the wave period. (*a*) $R_\delta = 1100$, (*b*) $R_\delta = 1414$.

$F_x = \langle \tau_x'^4 \rangle / \sigma_{\tau_x}^4$ along with the relative intensity $R_z = \sigma_{\tau_z}/\tau_0$ and the flatness coefficient $F_z = \langle \tau_z'^4 \rangle / \sigma_{\tau_z}^4$ of the spanwise component of the wall shear stress. In the following the time development of these statistics is examined in the light of the low-speed streaks dynamics previously discussed and of knowledge about these statistics for steady flows. Figure 20 shows the trend of the relative intensity R_x during a period. Both in the positive and in the negative half-cycle a time interval exists in which $|R_x|$ shows weak variations around a value close to 0.4. Such a time interval begins when the breakage of the low-speed streaks has occurred in all the fluid domain and ends near the flow reversal, when R_x diverges because of the vanishing of the wall shear stress. Comparing figure 20(*a*) with figure 20(*b*), it can be noted that when the Reynolds number increases the relative intensity is fairly constant in a longer time interval, while the value of the constant does not appreciably change. In the negative half-cycle (figure 20*a*), just after the flow reversal, another range of phases characterized by weak variations of $|R_x|$ around a value of 0.15 is observed. More specifically, for $\beta = 0.85$ and t in the range 3.3–4.2, $|R_x|$ varies within 0.12–0.16. Such a time interval corresponds to the phases in which the low-speed streaks are substantially straight and span all the computational domain, as shown in figure 9. Figure 20(*b*) shows that the width of this time interval decreases with Reynolds number as a larger portion of the cycle is occupied by well-developed turbulence, characterized by low-speed streaks that have already undergone the breaking process. A time interval with the previous characteristics also exists during the positive half-cycle, but it is very short because of the high acceleration, which quickly leads to the streaks instability and breaking. In the time that elapses between the two mentioned time intervals of rather constant value of R_x, the relative intensity increases, reaches a maximum and then stabilizes onto a value of about 0.4. Values of R_x close to 0.4 have also been reported by investigations on steady turbulent flows (Alfredsson & Johansson 1988; Durst, Jovanovic & Sender 1995; Obi *et al.* 1996). Therefore, it is expected that the turbulence exhibits characteristics similar to those of a steady flow when values of R_x close to 0.4 are observed during a time interval.

The relative intensity $R_z = \sigma_{\tau_z}/\tau_0$ of the wall shear stress in the spanwise direction is shown in figure 21. It can be observed that R_z has the same order of magnitude as R_x and a similar trend. When the streaks exhibit an elongated shape, $|R_z|$ takes values in the range 0.04–0.1, while after streaks breaking has occurred, it takes a value of approximately 0.25.

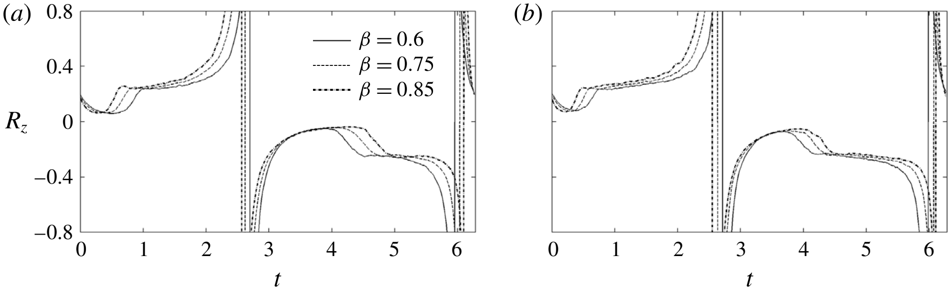

FIGURE 21. Relative intensity $R_z = \sigma_{\tau_z}/\tau_0$ of the wall shear stress along the z direction during the wave period. (a) $R_\delta = 1100$, (b) $R_\delta = 1414$.

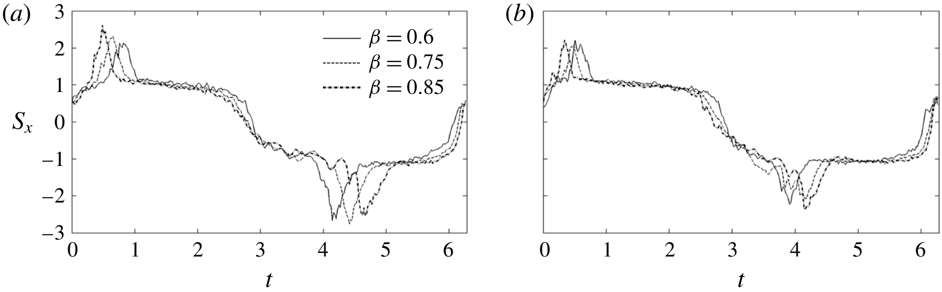

FIGURE 22. Skewness coefficient S_x of the wall shear stress along the x direction during a wave period. (a) $R_\delta = 1100$, (b) $R_\delta = 1414$.

Figure 22 shows that the skewness S_x of the wall shear stress in the streamwise direction is positive during the first half-cycle and negative during the second one. The rapid increase of S_x occurs during the final stage of the elongated streaks development, while the peak of S_x occurs at the onset of streaks breaking. In the positive half-cycle, when the breaking has occurred in all the fluid domain, S_x takes a value of approximately 1.1, then it slowly decreases attaining values slightly smaller than 1 before undergoing a rapid decrease near the flow reversal. On the other hand, in the negative half-cycle S_x almost immediately stabilizes to a value close to −1 after streaks breaking has occurred. An increase of R_δ causes a decrease of the peaks of S_x as the phase at which the streak breaking starts shifts back during the cycle, thus S_x has a shorter time to grow. Several studies (Alfredsson & Johansson 1988; Durst *et al.* 1995; Obi *et al.* 1996) reported that in steady turbulent flows the asymmetry of the wall shear stress takes values approximately equal to 1. The agreement of the present results with steady flow data confirms that there is a part of the cycle where the turbulence approximately evolves through a succession of quasi-steady states, as already suggested by the trend of R_x.

The trend of the flatness coefficient F_x is shown in figure 23. It is worth pointing out that the oscillations shown by F_x are due to the strong effect on this statistic of large values of the wall shear stress fluctuations. In order to smooth out such oscillations, the ensemble average should be computed on a very large number of flow cycles, at huge computational costs. Therefore, for the flatness coefficient even

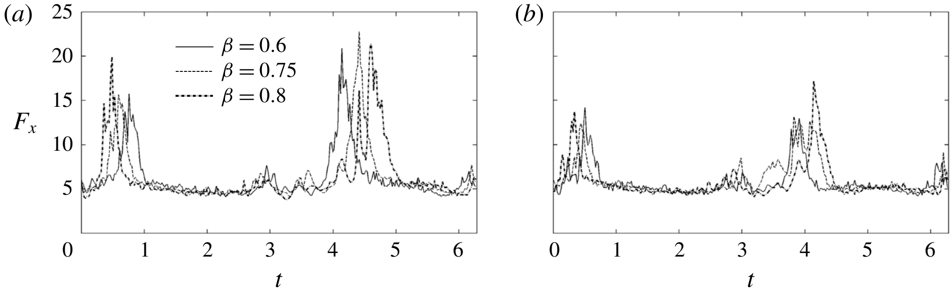

FIGURE 23. Flatness coefficient F_x of the wall shear stress along the x direction during a wave period. (a) $R_\delta = 1100$, (b) $R_\delta = 1414$.

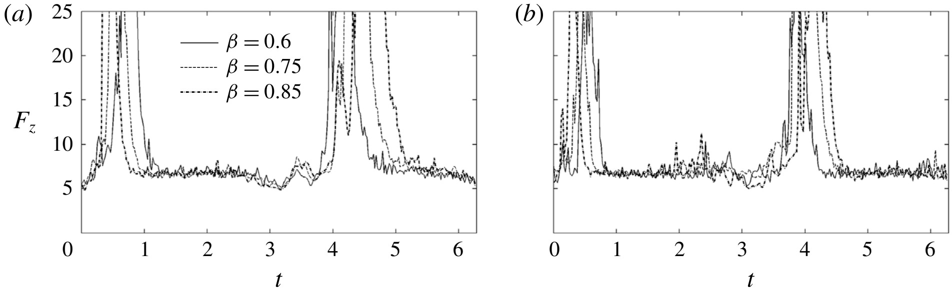

FIGURE 24. Flatness coefficient F_z of the wall shear stress along the z direction during a wave period. (a) $R_\delta = 1100$, (b) $R_\delta = 1414$.

trends contaminated by spikes have been accepted. As already observed for S_x, the rapid increase of F_x begins when the streaks still retain an elongated shape in the streamwise direction, while the peak of F_x occurs at the onset of the streak breaking. After breaking has occurred in the whole fluid domain, F_x takes a values of 5.4. However, afterwards F_x slowly decreases and takes a value of approximately 4.7 at $t = \pi/2$. An increase of the Reynolds number causes a decrease of the peaks in F_x for the same reason already explained regarding the skewness. As shown in figure 24, the trend of the flatness coefficient F_z is qualitatively similar to F_x but F_z is larger than F_x especially when elongated streaks are present. During these phases F_z can take values up to 40 in the positive half-cycle and up to 80 in the negative one. In figure 24 the larger values of F_z have been left outside from the range shown along the y-axis in order to focus more closely on the phases of well-developed turbulence, where F_z takes values of approximately 6.7. It can be also observed that when the Reynolds number increases the time intervals during which F_z is fairly constant increases. This is a common feature of all the statistics that have been examined here.

The probability density function of the dimensionless fluctuating wall shear stress τ'_x/σ_{τ_x} is shown in figure 25 for $\beta = 0.75$ and $R_\delta = 1100$. During the positive half-cycle negative fluctuations have a larger probability of occurrence than positive ones, the opposite is observed during the negative half-cycle. This behaviour is congruent with the trend of S_x during the cycle, shown in figure 22. For practical applications, such as those related to sediment transport predictions, it is useful to have an analytical expression describing the probability density of τ'_x/σ_{τ_x} at every phase. In this respect

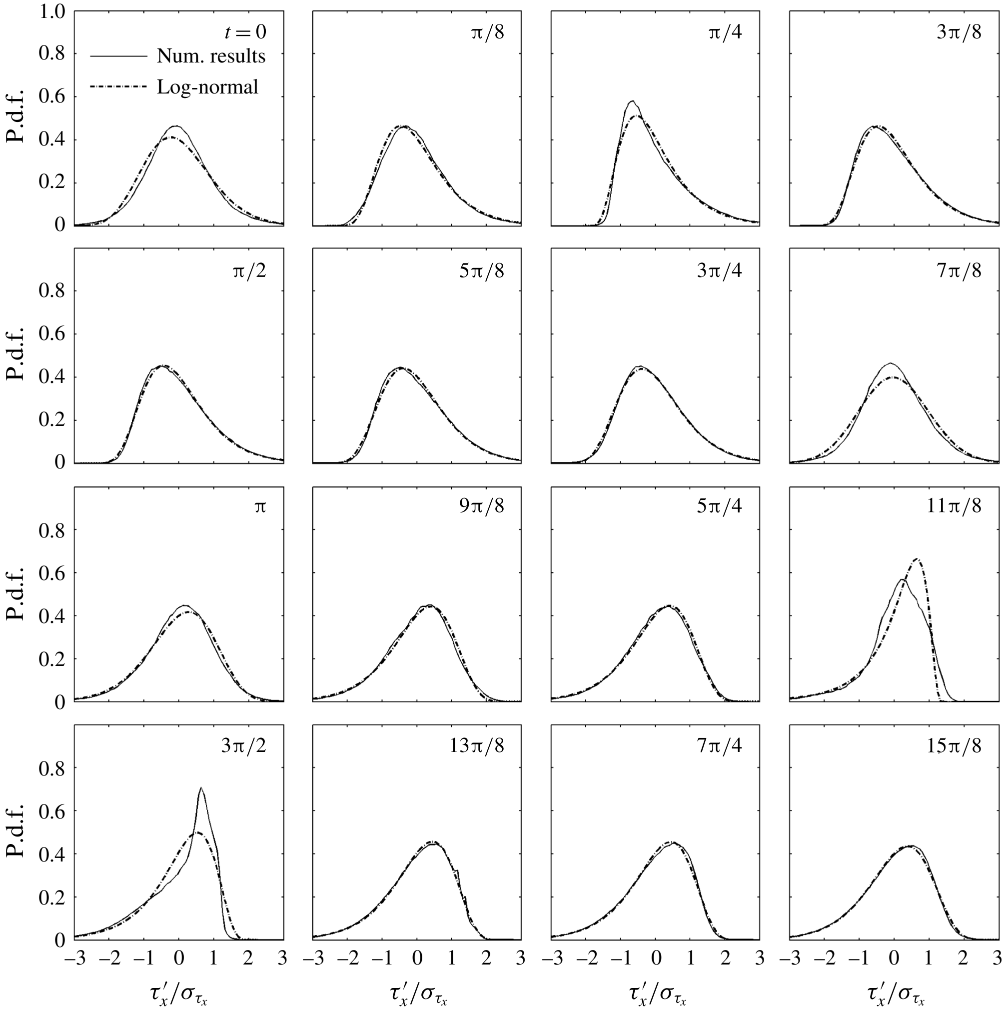

FIGURE 25. Probability density functions (p.d.f.) of the wall shear stress fluctuations along the x direction, τ'_x/σ_{τ_x}, at 16 phases during the cycle for $R_\delta = 1100$ and $\beta = 0.75$. Continuous lines show the numerical results while dashed lines show the log-normal probability density function that best fits to the numerical results.

the three parameter log-normal distribution fits rather well to the numerical results, as shown in figure 25. The log-normal distribution is given by the following expression:

$$p_{log}(\tau'_x/\sigma_{\tau_x}) = \frac{1}{(\tau'_x/\sigma_{\tau_x} - \tau_l)\sigma_y\sqrt{2\pi}} \exp\left[-\frac{1}{2}\left(\frac{\log(\tau'_x/\sigma_{\tau_x} - \tau_l) - \mu_y}{\sigma_y}\right)^2\right], \qquad (3.5)$$

where μ_y and σ_y are the mean and the standard deviation of $\log(\tau'_x/\sigma_{\tau_x} - \tau_l)$ respectively and τ_l is the location parameter. The parameters of (3.5) have been estimated by using the method outlined by Yevjevich (1982). Equating the skewness of the probability distribution to that of the numerical data S_x, the following expression for $\exp(\sigma_y^2)$ is obtained:

$$\exp(\sigma_y^2) = \left[1 + \frac{S_x}{2}(S_x + \sqrt{4 + S_x^2})\right]^{1/3} + \left[1 + \frac{S_x}{2}(S_x - \sqrt{4 + S_x^2})\right]^{1/3} - 1. \quad (3.6)$$

Then the parameters μ_y and τ_l are determined as follows:

$$\mu_y = \frac{1}{2}\log\left[\frac{\sigma^2_{\tau_x'/\sigma_{\tau_x}}}{\exp(\sigma_y^2)[\exp(\sigma_y^2) - 1]}\right], \quad (3.7)$$

$$\tau_l = \mu_{\tau_x'/\sigma_{\tau_x}} - \exp(\mu_y + 0.5\sigma_y^2), \quad (3.8)$$

where $\mu_{\tau_x'/\sigma_{\tau_x}}$ and $\sigma_{\tau_x'/\sigma_{\tau_x}}$ are the mean and the standard deviation of τ_x'/σ_{τ_x} respectively. Figure 25 shows that the most important discrepancies between the numerical results and the log-normal distribution occur at $t = \pi/4$, $t = 11\pi/8$ and $t = 3\pi/2$, which fall in the time intervals in which elongated streaks are present. Some discrepancies are also observed near the flow reversal at $t = 0$ and $t = 7\pi/8$.

The probability density function of τ_z/σ_{τ_z} shown in figure 26, is symmetric with respect to $\tau_z = 0$, since the probability of exceeding a value $\tau_z > 0$ is equal to the probability of not exceeding the value $-\tau_z$. In figure 24 the existence of time intervals in which the flatness of the wall shear stress is large was observed. This fact is reflected in the distribution of τ_z/σ_{τ_z}, which shows sharp peaks at some phases. Such a result is due to the high probability of finding values of τ_z in a small neighbourhood of $\tau_z = 0$ when breaking of low-speed streaks has not yet occurred over the entire fluid domain. The probability density function of τ_z/σ_{τ_z} can be described with a fairly good approximation by means of (3.9),

$$p(\tau_z/\sigma_{\tau_z}) = \frac{1}{\sqrt{2\gamma - 3}B(\gamma - 1/2, 1/2)}\left[1 + \left(\frac{\tau_z/\sigma_{\tau_z}}{\sqrt{2\gamma - 3}}\right)^2\right]^{-\gamma}, \quad (3.9)$$

which is a modification of the Pearson type VII distribution (Johnson, Kotz & Balakrishnan 1995). In (3.9) the condition that the variance of τ_z/σ_{τ_z} is equal to 1 is already imposed, B is the beta function and γ is the parameter of the distribution, which must be larger than 3/2. Here, γ has been determined by means of the maximum likelihood method. Figure 26 shows that the numerical results are in a fairly good agreement with (3.9), except at the phases $\pi/4$ and $3\pi/2$, in which the breaking of streaks is in progress and the probability density exhibits a sharp peak. It is worth highlighting that the flatness provided by (3.9) is finite only if γ is larger than 5/2 and that in figure 26 this condition is violated at $t = \pi/4$, $t = 11\pi/8$ and $t = 3\pi/2$. In order to improve the description of the numerical results at phases $\pi/4$ and $3\pi/2$, a generalization of the normal distribution can be employed,

$$p(\tau_z/\sigma_z) = \frac{1}{2}\frac{\alpha\Gamma^{1/2}(3/\alpha)}{\Gamma^{3/2}(1/\alpha)}\exp\left[-\left(\frac{\Gamma(1/\alpha)}{\Gamma(3/\alpha)}\right)^{-\alpha/2}(|\tau_z/\sigma_z|)^{\alpha}\right], \quad (3.10)$$

where Γ is the gamma function and α is the parameter of the distribution. Equation (3.10) is shown by markers in figure 26 at the phases $\pi/4$ and $3\pi/2$. It can be observed that the agreement with the numerical data is improved compared to that of (3.9). However, the results at $t = 13\pi/8$ show that the shape of the probability density

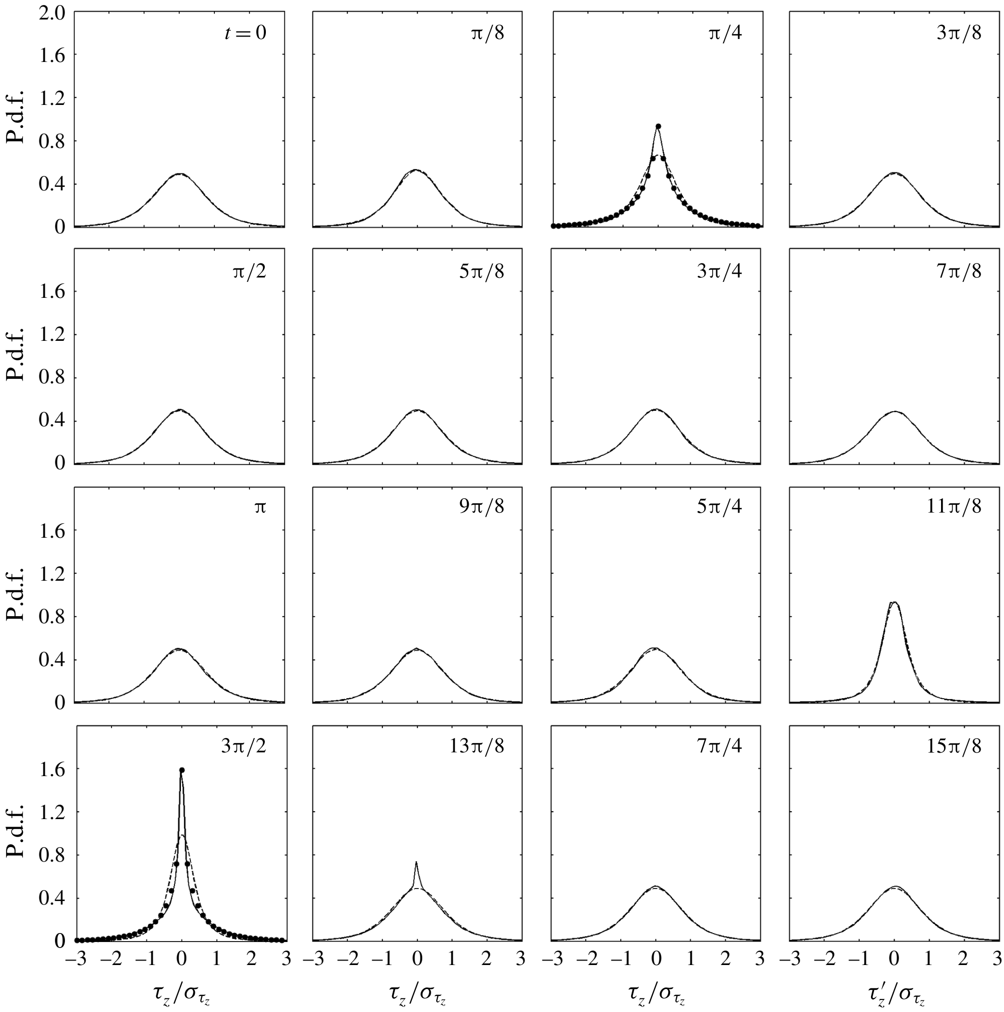

FIGURE 26. Probability density functions (p.d.f.) of the wall shear stress τ_z/σ_{τ_z} along the z direction at 16 phases during the cycle for $R_\delta = 1100$ and $\beta = 0.75$. Continuous lines show the numerical results while dashed lines show the Pearson distribution type VII (3.9) that best fits to the numerical results. The curves denoted by dots at the phases $\pi/4$ and $3\pi/2$ are described by (3.10).

may be rather complicated, indeed at this phase (3.9) provides a good description of the probability density except in a neighbourhood of $\tau_z/\sigma_z = 0$, where the probability density shows a sharp peak and could be better described by (3.10).

Finally, we tackle the issue arisen in connection with figure 19, concerning the observation that large values of the spanwise wall shear stress seem to occur simultaneously with positive fluctuations of the streamwise wall shear stress. In order to address this issue, we write the probability density function as follows:

$$p(\tau_z) = \psi_1 + \psi_2, \tag{3.11}$$

$$\psi_1 = p(\tau_z \mid \tau_x' > 0) \times p(\tau_x' > 0), \tag{3.12}$$

$$\psi_2 = p(\tau_z \mid \tau_x' < 0) \times p(\tau_x' < 0), \tag{3.13}$$

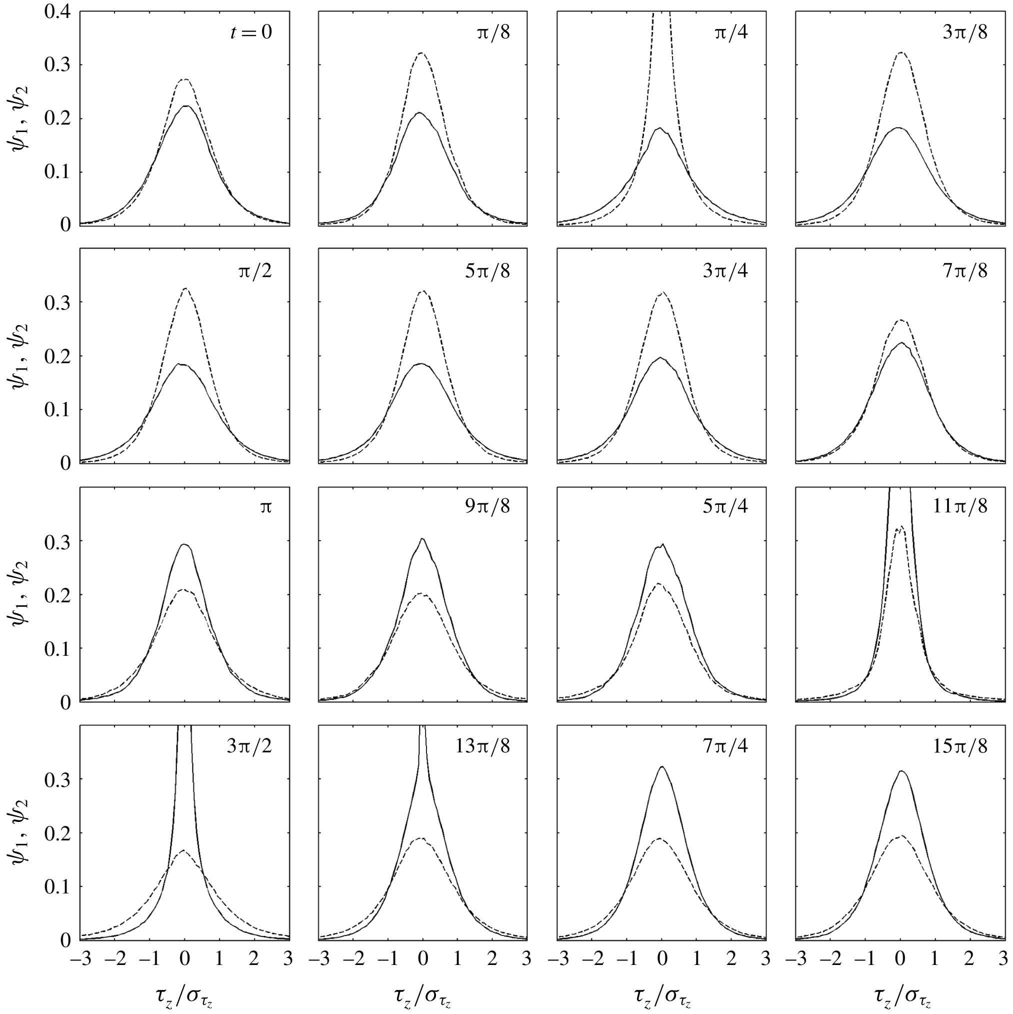

FIGURE 27. Trend of the functions ψ_1 and ψ_2 (see (3.11)–(3.13)) at 16 phases during the cycle for $R_\delta = 1100$ and $\beta = 0.75$; continuous lines: ψ_1; dashed lines: ψ_2.

where the vertical bar means ‘conditioned to’. The functions ψ_1 and ψ_2 are the contributions to the probability density function of τ_z of events characterized by $\tau_x' > 0$ and $\tau_x' < 0$ respectively. The function ψ_1 and ψ_2 are plotted in figure 27 in order to gain insights about the contributions of the two kind of events to the probability density of τ_z. Figure 27 shows that, in the positive half-cycle, small values of the spanwise wall shear stress occur more frequently in concomitance with negative fluctuations of the streamwise wall shear stress, while large values occur more frequently simultaneously with positive fluctuations. Such behaviour is amplified when the breaking of streaks is in progress, as occurring at phases π/4 and 3π/2. Note that in the negative half-cycle the role of the functions ψ_1 and ψ_2 is inter-changed with respect to the positive half-cycle. Another result that emerges from figure 27 is that, in the positive half-cycle, the peakedness of the probability density function is mainly due to values of the wall shear stress occurring simultaneously with negative fluctuations of the streamwise wall shear stress, while the opposite is observed in the negative half-cycle.

4. Conclusions

In this paper the hydrodynamics of wall-bounded acceleration-skewed oscillatory flows has been studied by means of numerical integration of the Navier–Stokes equations. Even though the flow is not velocity skewed in the irrotational region, it becomes velocity skewed in the boundary layer, causing an asymmetry between the peaks of the wall shear stress in the two half-cycles. Such an asymmetry increases with acceleration skewness while an increase of Reynolds number from the laminar regime causes first a decrease and then an increase. For $\beta = 0.75$ the minimum value of the asymmetry is at approximately $R_\delta = 925$.

During the accelerating phase, the near-wall region is characterized by turbulent structures consisting in low- and high-speed streaks of fluid. As long as the streaks remain substantially straight and aligned with the flow direction, they do not cause significant deviations of the wall shear stress from the laminar values. Before the end of the accelerating phase, the streaks become unstable and break into short segments which eventually coalesce during the decelerating phase. The break up does not occur everywhere at the same instant, but in a progressive manner and it is accompanied by a rapid increase of the wall shear stress.

The time derivative of the turbulent kinetic energy, integrated over the boundary layer, increases during the accelerating phase up to a maximum which occurs near the start of the streaks breaking. Just after the onset of breaking, small-scale turbulent structures, characterized by a remarkable dissipative capability, are generated, resulting in a significant decrease of the time derivative of turbulent kinetic energy. Because of the acceleration skewness, the period-averaged Reynolds stress does not vanish. Under such a circumstance the balance of the period-averaged momentum is satisfied as a result of the viscous stress generated by a steady streaming directed against the largest acceleration. Such a steady streaming increases with acceleration skewness and decreases with Reynolds number. In water tunnels used in several investigations related to the present subject (Jensen *et al.* 1989; van der A *et al.* 2011), because of the finite longitudinal dimension of the facility, the overall flow rate due to the steady streaming is balanced by a return current. While the steady streaming is driven by the gradient of the period-averaged Reynolds stress, the return current is driven by a pressure gradient. Due to this fundamental difference between the two flows, the steady streaming does not exert a friction on the wall while the return current does induce a steady friction in opposite direction of the steady streaming.

The relative intensity R_x and the skewness S_x of the streamwise wall shear stress take values of approximately 0.4 and 1 respectively during relatively large time intervals that begin when the streaks breaking has occurred in the entire fluid domain. The width of such time intervals increases with the Reynolds number while the phase of the onset depends on both the Reynolds number and the acceleration skewness. The agreement between these statistical parameters and those observed in steady turbulent flows, allows to infer that during the these time intervals the turbulence approximately evolves through a succession of quasi-steady states. The relative intensity R_z of the wall shear stress in the spanwise direction has the same qualitative behaviour and the same order of magnitude as R_x, but in general R_x is larger than R_z. The flatness coefficient of both the streamwise and spanwise component of the wall shear stress is large, especially when elongated streaks are present in the flow. After streak break down the flatness takes values of approximately 5.4 and 6.7 for the streamwise and spanwise components respectively. The analysis has also shown that the peak of the skewness occurs at the onset of the streak breaking. Since the turbulent spots (Carstensen *et al.* 2010) are those regions of the fluid domain where breaking has already occurred, the peak of S_x also defines the onset of the turbulent spots during the flow cycle.

The probability density function of the wall shear stress in the streamwise direction is well described by a log-normal distribution. The probability density of the wall shear stress in the spanwise direction can be well approximated by a Pearson type VII distribution, except during streak breaking, when the coexistence of quasi-laminar and turbulent regions generates a sharp peak in the probability density. When this occurs, a generalized normal distribution provides a better agreement with the numerical data than the Pearson distribution. Finally, it is shown that low absolute values of the spanwise wall shear stress occur more frequently in concomitance with negative fluctuations of the streamwise wall shear stress, while large values occur more frequently simultaneously with positive fluctuations.

Present findings are a first order of approximation of the flow under real field conditions, where the spatial variability due to the sea waves may have an impact on the boundary layer. In addition, when the bed is rough, the low-speed streak development and breaking as well as the statistics of the wall shear stress may be different from those of a smooth bed. Therefore, including these effects in the analysis of the boundary layer represents an interesting development of this work aimed at providing results closer to field conditions.

Acknowledgements

This research has been partially funding by the Ministero dell'Istruzione, dell'Università e della Ricerca through the PRIN 2012 Project 'Hydromorphodynamic modeling of coastal processes for engineering purposes'. The authors wish to thank the anonymous referees who provided valuable comments that helped to improve the manuscript.

REFERENCES

van der A, D. A., O'Donoghue, T., Davies, A. & Ribberink, J. S. 2011 Experimental study of the turbulent boundary layer in acceleration-skewed oscillatory flow. *J. Fluid Mech.* **684**, 251–283.

van der A, D. A., O'Donoghue, T., Davies, A. & Ribberink, J. S. 2010 Measurements of sheet flow transport in acceleration-skewed oscillatory flow and comparison with practical formulations. *Coast. Engng* **57**, 331–342.

Abreu, T., Michallet, H., Silva, P., Sancho, F., van der A, D. A. & Ruessink, B. 2013 Bed shear stress under skewed and asymmetric oscillatory flows. *Coast. Engng* **73**, 1–10.

Alfredsson, P. H. & Johansson, A. 1988 The fluctuating wall-shear stress and the velocity field in the viscous sublayer. *Phys. Fluids* **32** (5), 1026–1033.

Blondeaux, P., Vittori, G., Lalli, F. & Pesarino, V. 2012 Steady streaming and sediment transport at the bottom of sea waves. *J. Fluid Mech.* **697**, 115–149.

Calantoni, J. & Puleo, J. 2006 Role of pressure gradient in sheet flow of coarse sediments under sawtooth waves. *J. Geophys. Res. Oceans* **111**, C01010.

Carstensen, S., Sumer, B. M. & Fredsøe, J. 2010 Coherent structures in wave boundary layers. Part 1. Oscillatory motion. *J. Fluid Mech.* **646**, 169–206.

CAVALLARO, L., SCANDURA, P. & FOTI, E. 2011 Turbulence-induced steady streaming in an oscillating boundary layer. *Coast. Engng* **58**, 290–304.

CORINO, E. R. & BRODKEY, R. S. 1969 A visual investigation of the wall region in turbulent flow. *J. Fluid Mech.* **37**, 1–39.

COSTAMAGNA, P., VITTORI, G. & BLONDEAUX, P. 2003 Coherent structures in oscillatory boundary layers. *J. Fluid Mech.* **474**, 1–33.

DIBAJNIA, M. & WATANABE, A. 1998 Transport rate under irregular sheet flow conditions. *Coast. Engng* **35**, 167–183.

DONG, L., SATO, S. & LIU, H. 2013 A sheetflow sediment transport model for skewed-asymmetric waves combined with strong opposite currents. *Coast. Engng* **71**, 87–101.

DRAKE, T. & CALANTONI, J. 2001 Discrete particle model for sheet flow sediment transport in the nearshore. *J. Geophys. Res. Oceans* **106** (C9), 19859–19868.

DURST, F., JOVANOVIC, J. & SENDER, J. 1995 LDA measurments in the near-wall region of a turbulent pipe flow. *J. Fluid Mech.* **295**, 305–335.

ELGAR, S., GUZA, R.-T. & FREILICH, M. 1988 Eulerian measurements of horizontal accelerations in shoaling gravity waves. *J. Geophys. Res.* **93**, 9261–9269.

FISHLER, L. S. & BRODKEY, R. S. 1991 Transition, turbulence and oscillating flow in a pipe. *Exp. Fluids* **11**, 388–398.

FUHRMAN, D. R., FREDSØE, J. & SUMER, B. 2009 Bed slope effects on turbulent wave boundary layers: 2. Comparison with skewness, asymmetry, and other effects. *J. Geophys. Res.* **114**, 19.

HAMILTON, J., KIM, J. & WALEFFE, F. 1995 Regeneration mechanisms of near-wall turbulence structures. *J. Fluid Mech.* **287**, 317–348.

HOLMEDAL, L. & MYRHAUGH, D. 2006 Boundary layer flow and net sediment transport beneath asymmetrical waves. *Coast. Engng* **26**, 252–268.

HSU, T. & HANES, D. 2004 Effects of wave shape on sheet flow sediment transport. *J. Geophys. Res. Oceans* **109** (C05025), 15.

JENSEN, B. L., SUMER, B. M. & FREDSØE, J. 1989 Turbulent oscillatory boundary layers at high Reynolds numbers. *J. Fluid Mech.* **206**, 265–297.

JEONG, J. & HUSSAIN, F. 1995 On the identification of a vortex. *J. Fluid Mech.* **285**, 69–74.

JOHNSON, N., KOTZ, S. & BALAKRISHNAN, N. 1995 *Continuous Univariate Distributions*, vol. 2. Wiley.

KIM, J. & MOIN, P. 1985 Application of a fractional-step method to incompressible Navier–Stokes equations. *J. Comput. Phys.* **59**, 308–323.

KING, D. 1990 Studies in oscillatory flow bed load sediment transport. PhD thesis, University of California, San Diego.

KLINE, S. J., REYNOLDS, W. C., SCHRAUB, F. A. & RUNSTADLER, P. W. 1967 The structure of turbulent boundary layer. *J. Fluid Mech.* **30**, 741–773.

MADSEN, O. 1974 Stability of a sand bed under breaking waves. In *Proc. 14th Conf. on Coastal Engineering*, pp. 776–794. ASCE.

MOIN, P. & MAHESH, K. 1998 Direct numerical simulation: a tool in turbulence research. *Annu. Rev. Fluid Mech.* **30**, 539–578.

NIELSEN, P. & CALLAGHAN, D. 2003 Shear stress and sediment transport calculations for sheet flow under waves. *Coast. Engng* **47**, 347–354.

OBI, S., INOUE, K., FURUKAWA, T. & MASUDA, S. 1996 Experimental study on the statistics of wall shear stress in turbulent channel flow. *Intl J. Heat Fluid Flow* **17**, 187–192.

O'DONOGHUE, T. & WRIGHT, S. 2004 Flow tunnel measurements of velocities and sand flux in oscillatory sheet flow for well-sorted and graded sands. *Coast. Engng* **51**, 1163–1184.

OZDEMIR, C. E., HSU, T. J. & BALACHANDAR, S. 2014 Direct numerical simulations of transition and turbulence in smooth-walled Stokes boundary layer. *Phys. Fluids* **26**, 25.

PEDOCCHI, F., CANTERO, M. & GARCIA, M. 2011 Turbulent kinetic energy balance of an oscillatory boundary layer in the transition to the fully turbulent regime. *J. Turbul.* **12** (32), 1–27.

POPE, S. B. 2000 *Turbulent Flows*. Cambridge University Press.

RIBBERINK, J. & AL-SALEM, A. 1995 Sheet flow and suspension of sand in oscillatory boundary layers. *Coast. Engng* **25**, 205–225.

ROBINSON, S. K. 1991 Coherent motions in the turbulent boundary layer. *Annu. Rev. Fluid Mech.* **23**, 601–639.

SALON, S., ARMENIO, V. & CRISE, A. 2007 A numerical investigation of the Stokes boundary layer in the turbulent regime. *J. Fluid Mech.* **570**, 253–296.

SCANDURA, P. 2007 Steady streaming in a turbulent oscillating boundary layer. *J. Fluid Mech.* **571**, 265–280.

SCANDURA, P. 2013 Two-dimensional vortex structures in the bottom boundary layer of progressive and solitary waves. *J. Fluid Mech.* **728**, 340–361.

SCANDURA, P. & FOTI, E. 2011 Measurements of wave-induced steady currents outside the surf zone. *J. Hydraul. Res.* **49** (S1), 64–71.

SCANDURA, P., FOTI, E. & FARACI, C. 2012 Mass transport under standing waves over a sloping beach. *J. Fluid Mech.* **701**, 460–472.

SCHOPPA, W. & HUSSAIN, F. 2002 Coherent structures generation in the near-wall turbulence. *J. Fluid Mech.* **453**, 57–108.

SILVA, P., ABREU, T., VAN DER A, D. A., SANCHO, F., RUESSINK, B., VAN DER WERF, J. & RIBBERINK, J. S. 2011 Sediment transport in nonlinear skewed oscillatory flows: Transkew experiments. *J. Hydraul. Res.* **49**, 72–80.

TROWBRIDGE, J. & MADSEN, O. 1984 Turbulent wave boundary layer 2: second order theory and mass transport. *J. Geophys. Res. Oceans* **89** (C5), 7999–8007.

VITTORI, G. & VERZICCO, R. 1998 Direct simulation of transition in an oscillatory boundary layer. *J. Fluid Mech.* **371**, 207–232.

WATANABE, A. & SATO, S. 2004 A sheet-flow transport rate formula for asymmetric forward-leaning waves and currents. In *Proc. 19th Coastal Engng Conf.*, pp. 1703–1714. ASCE.

YEVJEVICH, V. 1982 *Probability and Statistics in Hydrology*. Water Resources Publications.